IJP

Resonance Raman scattering on one-dimensional systems

M S Dresselhaus**, G Dresselhaus†*, A M Rao***, A Jorio†‡, A G Souza Filho††,
Ge G Samsonidze** and R Saito****

**Department of Physics and Department of Electrical Engineering and Computer Science,
Massachusetts Institute of Technology, Cambridge, MA 02139

† Francis Bitter Magnet Laboratory, Massachusetts Institute of Technology,
Cambridge, MA 02139

***Department of Physics, Clemson University, Clemson, SC 29634-0978

†† Departamento de Física, Universidade Federal de Minas Gerais,
Belo Horizonte, MG, 30123-970 Brazil

††Departamento de Física, Universidade Federal do Ceará, Fortaleza-CE,
60455-760, Brazil

****Department of Electronic Engineering, University of Electro-Communications,
and CREST JST, Tokyo, 182-8585, Japan

Abstract   A review of the resonance Raman effect in one-dimensional (1D) system is presented Due to the strong electron-phonon coupling and the quantum confinement of electrons and phonons in 1D systems, interesting effects are observed, such as asymmetries in the Stokes/anti-Stokes spectra and line-shape dependence on satisfying the resonance condition. Analysis of these effects give detailed information about the confined phonon and electron states, showing that resonance micro-Raman spectroscopy of phonon modes can determine electronic and structural properties of 1D-systems. The single wall carbon nanotube (SWNT) is used as a prototype 1D system for describing resonance Raman scattering in 1D, since many experimental results are now available for this system at the single nanotube level, and because detailed theoretical modeling can be carried out for this system. The results on SWNTs should provide a valuable guide for Raman studies on other 1D systems. It is also shown that the resonance Raman effect provides a useful technique for obtaining phonon dispersion relations for nanoscale samples, and that measurements on low dimensional systems can be used to obtain important information about related higher dimensional systems that is otherwise difficult to obtain

1. Historical Introduction

The concept of light scattering first intrigued Sir C. V. Raman when he observed the wonderful blue opalescence of the Mediterranean sea during his voyage to Europe in 1921. After returning to Calcutta, much of his work during 1922—1927 focused on determining the connection between the state of polarization of the scattered light in fluids and the optical anisotropy of the molecules. In April 1923, he experimentally discovered for the first time that, besides the Rayleigh type of molecular light scattering, another extremely feeble type of secondary radiation existed whose wavelength was different from the primary or incident radiation. Highly purified samples of alcohols and glycerine obtained from repeated slow distillation the liquid in vacuum, consistently showed, in every case,

that the color of the scattered light was different from that of the incident light and was red-shifted in frequency. These secondary radiations were also strongly polarized, which allowed Raman to realize that the observations made in his laboratory were an optical analogue of Compton effect. Raman also realized that his scattering experiments with visible light at 500 nm will differ in intensity by several orders of magnitude when compared to Compton's experiments with x-rays (wavelength of 0.7 nm), since one of the characteristics of inelastic photon scattering is that the intensity of light scales to the fourth power of the photon energy. This difficulty was overcome by using a 7 inch refracting telescope in combination with a short-focus lens to condense sunlight into a narrow intense beam suitable for spectroscopy [see Figure 1(b)] [1].

In subsequent experiments, Raman used the monochromatic radiations from a mercury arc as the primary source of radiation,

†Corresponding Author

and he was successful in capturing the spectrum of liquid carbon tetrachloride CCl_4 on a photographic film [Figure 1(a)] which included a number of sharp lines or bands on a diffuse background which were absent in the light of the mercury arc [1]. Using the Compton effect in which the conservation of energy and momentum principles hold as a guide for the interpretation of his light scattering experiments, it at once became clear to Raman that, if the scattering particle gains energy during the encounter with the photon, the latter is deprived of energy to the same extent, and accordingly is red-shifted in frequency [1]

435X Å

4046 Å

(a)   (b)
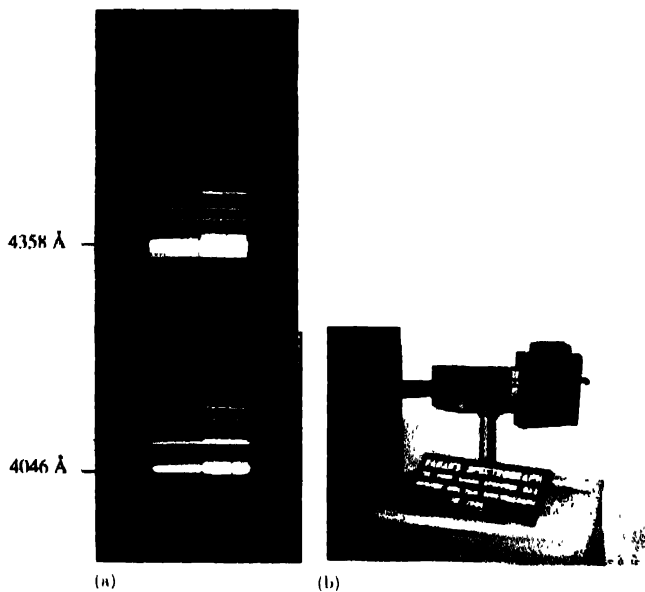
Figure 1. (a) Raman spectrum of carbon tetrachloride recorded on photographic film and (b) original Raman apparatus used by Sir C V Raman [1]

Raman's interest in carbon-related materials began with CCl_4 which exhibited sufficiently strong Raman lines so that a spectrum could be recorded [Figure 1(a)]. Raman was always interested in finding materials that showed a strong Raman effect. Thus a life-long interest in diamond developed for Raman, when his younger brother who had just graduated in physics, made a brief spectroscopic examination of his wedding diamond ring, and found that it exhibited strong and sharp Raman lines corresponding to the now well-known frequency shift of 1332 cm^{-1}. Figure 2 shows two examples of the Raman spectra of diamond obtained by Raman and his colleagues at increasing exposure times [2, 3]. Raman was struck by the appearance of sharp lines in the spectrum, since he knew that molecules exhibited sharp lines and bulk diamond couldn't be viewed as a "giant molecule". Based on a detailed theoretical model which Raman developed [3], he concluded that a crystal can be viewed as a collection of independent, non-interacting supercells, as far as the optic modes of vibrations are concerned. This is similar to how we now view light scattering from crystalline solids, 75 years later.

The universality of Raman scattering phenomenon and the present ease of this experimental technique enable Raman spectroscopy to provide an insight into the ultimate structure of the scattering substance.

(a)   (b)
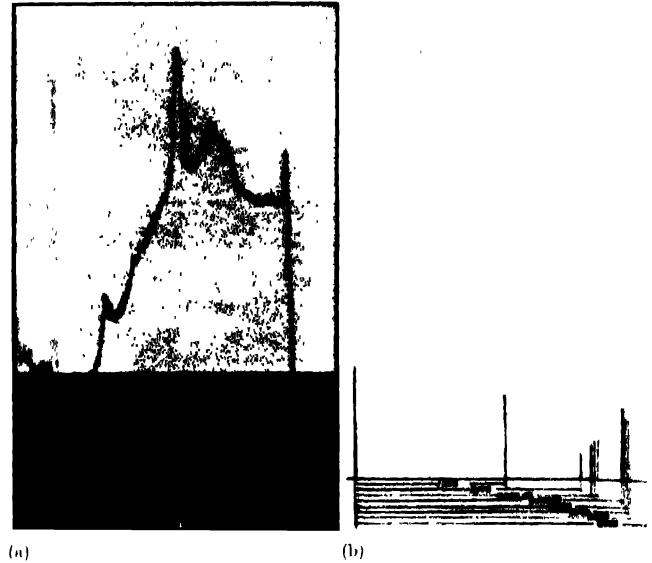
Figure 2. (a) Raman spectrum of diamond [2, 3] (b) A schematic of phonons involved in Raman scattering from diamond. Note that Raman himself recognized that harmonics and combination modes should also be observed.

Even though the first experiments by Sir C.V. Raman on the inelastic scattering of light were reported 75 years ago, and the field has been very active over the intervening years, new directions for Raman spectroscopy continue to emerge as science progresses. We report here one recent new direction brought about by the availability of one-dimensional systems at the nanoscale, the new science they offer, and the highly sensitive probe that Raman spectroscopy provides to investigate, one-dimensional systems such as single wall carbon nanotubes, at the single nanotube level [4].

## 2. Electrons and phonons in one-dimensional systems

The Raman spectroscopy of molecules is now very well developed, going back to the pioneering work of Sir C. V. Raman and the fertile research field that this work generated [5]. In terms of dimensionality considerations, molecules can be regarded as a zero-dimensional (0D) quantum dot system. The Raman spectra for 0D molecular systems are very rich, showing hundreds perhaps thousands of sharp lines for vibration-rotational levels, and many harmonics and combination modes can be resolved and quantitatively interpreted, with Raman spectra observed at the molecular level [5].

Unlike 0D molecules, 3D and 2D solids inelastically scatter light through the interaction of the photons with the collective lattice vibrations or phonons, and not through the scattering by individual vibrational and rotational modes of the constituent

atoms or molecules. In 0D molecules, the individual vibrational and rotational levels are well separated in energy, thus giving rise to many combination modes and overtones that can be resolved in the Raman spectrum. The situation is quite different in 3D and 2D solids, where there is a quasi-continuum of energy states, so that the individual Raman scattering transitions are not well separated in energy, but rather form broad features in the Raman spectrum. Thus, the Raman spectra for 3D and 2D solids exhibit much broader Raman spectral features in the first-order spectra, and the harmonics and combination mode features tend to be very broad, of low intensity, and generally contribute a broad background scattering rather than a resolvable line spectrum. In this article we show that resonance Raman spectra for one-dimensional systems, are quite different from that for 2D and 3D solid state systems, insofar as 1D systems provide a much richer Raman spectra than their 2D and 3D counterparts, but at the same time the 1D resonance Raman spectra are strongly influenced by the quasi-continuum 1D states where phonon dispersion $\omega_{ph}(q)$ occurs.

We start our discussion by describing what we mean by 1D or 2D systems. In 3D space, a 1D system is not strictly one-dimensional, nor is a 2D system strictly two-dimensional, but these low-dimensional systems have a finite (nano-scale) length L in the direction(s) perpendicular to the periodic 1D or 2D directions. In the nanoscale direction, the wavevector is quantized as $(2\pi / L)p$ where p is a subband index ($p = 1, 2, 3, \ldots p_{max}$) where p_{max} is given by L/a and a is the lattice constant of 2D graphite. By considering L to be of nm length, the number of allowed states p is small ($p_{max} \sim 10$), so that quantum effects (also called quantum confinement effects) become important. Each value of p denotes a good physical quantum number for describing the 1D and 2D energy subbands for electrons and phonons. Thus the 1D subbands are described from the 2D energy band by cutting the 2D Brillouin zone by parallel lines aligned in the direction of the nanoscale dimension. Along the continuous direction, such as the length of a nanowire or a nanotube, the quasi-continuous wavevector k is given by $-\pi / T < k < \pi / T$ where T is the lattice constant of the nanotube. The nanotube potential $V(r)$ exhibits 1D periodicity along a macroscopic lengthscale, which might typically be of μm size. When we consider 1D subbands as coming from a 3D energy band structure (or 2D subbands from a 3D energy band structure), we can consider parallel cutting planes to reduce the dimensionality, as illustrated in Figure 3, where the energy-momentum contours are shown for the valence and conduction bands, each obeying a linear dependence of energy on wave vector and forming a degenerate point where the two bands touch to define a zero gap semiconductor (as in 2D graphite). The planes cutting these contours denote the dispersion relation of the 1D system derived from the 2D system, each cutting plane giving rise to a different subband. The extrema in each cutting planes gives the wave vector and energy for the van Hove singularity (k_j, E_j).

Electrons likewise behave quite differently in systems of different dimensionality. For example, the electronic density of
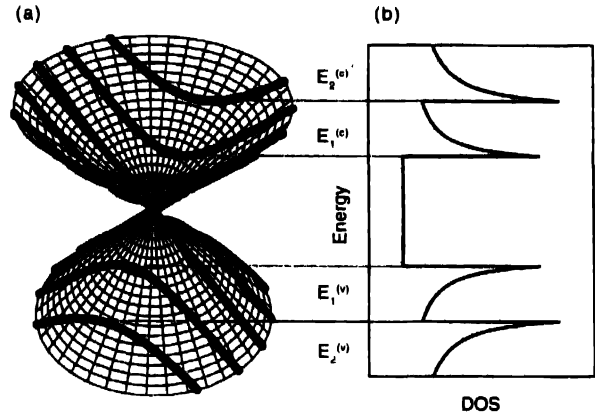

Figure 3. (a) The energy-momentum contours for the valence and conduction bands for a 2D system, each band obeying a linear dependence of energy on wave vector and forming a degenerate point where the two bands touch to define a zero gap semiconductor. The planes cutting these contours denote the dispersion relation for the 1D system derived from the 2D system. Each cutting plane gives rise to a different subband. The extrema in each cutting planes gives the wave vector and energy for the van Hove singularity (k_j, E_j). The energies $E_i^{(v)}$ and $E_i^{(c)}$ for valence and conduction bands are indicated on the figure and the corresponding wavevectors at the van Hove singularities are $k_j^{(v)}$ and $k_j^{(c)}$. (b) The 1D density of states for the conduction and valence bands corresponding to the $E(k)$ dispersion relations for the subbands shown in (a)

states (DOS) profiles for systems of different dimensionality (3D, 2D, 1D, and 0D) are very different, as shown in Figure 4. In general the density of states profiles can be represented as

$$\rho(E) = \begin{cases} 0 & \text{for } E < E_j \\ C(E - E_j)^{\frac{d-2}{2}} & \text{for } E_j > E \end{cases} \quad (1)$$

where d denotes the dimensions and assumes the values 1, 2, and 3, respectively, for 1D, 2D and 3D systems. Here E_j can be considered as a critical energy in the density of states. For a 3D system E_j might correspond to an energy threshold for the onset of optical transitions, or to a band edge state in a semiconductor. For a 1D system, E_j would correspond to a van Hove singularity in the density of states occurring at each subband edge, where the magnitude of the electronic density of states becomes very large.

In contrast to 3D and 2D systems, 1D systems exhibit DOS profiles which are more similar to the case of 0D systems (see Figure 4), having very sharp maxima at certain energies and a
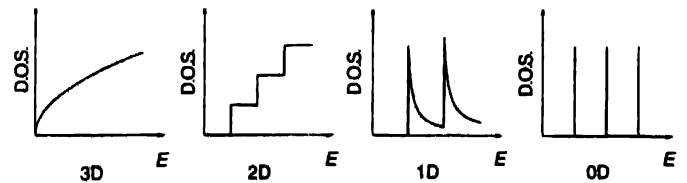
Figure 4. Typical density of states for 3D, 2D, 1D and 0D systems.

rather low DOS magnitude between the maxima. Thus, it is to be expected that 1D systems would be much richer in their resonance Raman spectra than 3D and 2D solids, where the many levels are all smeared out into spectral bands. We would thus expect 1D systems to show Raman spectra similar to those of 0D molecules, i.e., having many combination Raman bands and overtones.

A single wall carbon nanotube (SWNT) is both a molecule and a very special 1D system. Since the cross-section is a cylinder only one atom in thickness, it should be closely related to 0D molecules. Although nanotubes have lengths that can span hundreds of μm and therefore exhibit a continuum electron and phonon spectra in the continuum direction, nevertheless the nanotubes behave like individual molecules, insofar as every nanotube that has a different diameter and chirality, can be considered as a distinct molecule with a distinct Raman spectrum, as we show in §4. The resonance Raman spectra for SWNTs do indeed show well-resolved overtones and combination modes in the Raman spectra. Nanowires, in contrast, cannot in general be considered as distinct molecules, for which the location of every atom can be specified, and this is so because the lateral surfaces of a nanowire are in general not uniquely specified. The present review focuses mostly on the transition from 3D to 1D systems, and on how such a transition affects Raman spectroscopy.

Because of advances in modern technology, it is now possible to both fabricate such 1D systems and to characterize them, and also to control process parameters so that the transition between low dimensional and 3D systems can be investigated. If the low dimensional systems have the same crystal structure as the bulk parent material, the electronic states of the low dimensional structure can be obtained as a subset of the electronic states of the bulk counterpart. Considering wavevectors of the electronic states in the reciprocal space of the bulk material, all the wavevectors within the first Brillouin zone are allowed. However, when we move to the case of low dimensional structures, the structural lengths in the nanoscale directions contain only tens of atoms, so that quantum effects become important. The electronic wavevectors in these nanoscale directions become quantized, in order to maintain an integer number of wave function nodes along the nanoscale directions, in accordance with quantum theory. Thus, the reciprocal space of the bulk parent material is quantized in the nanoscale directions The number of quantized states is equal to the number of unit cells of the bulk parent material which is needed to construct a unit cell of the low dimensional structure. For example, if one grows a thin film from a bulk three-dimensional crystal, the electronic states for the thin film can be constructed from the three-dimensional reciprocal space of the parent bulk material as wavevectors lying in certain parallel equidistant planes. This is an extended representation of the two-dimensional reciprocal space of the thin film, where each

electronic energy subband from the two-dimensional reciprocal space corresponds to a different plane in the three-dimensional reciprocal space of the parent bulk material.

Similarly, when one-dimensional nanotubes are rolled up from the two-dimensional sheets of the three-dimensional layered bulk materials, such as graphite, boron nitride, or a transition metal dichalcogenide, different subbands in the one-dimensional reciprocal space of the nanotube can be expanded into the two-dimensional reciprocal space of a single sheet of the bulk layered material as a set of the parallel equi-distant lines. These lines are known as "cutting lines," and the method of constructing the one-dimensional electronic energy subbands by cutting the two-dimensionalel ectronic dispersion relations with these lines is known as the "zone-folding" method [6]. In the case of a nanotube 1D system, the total number of the cutting lines for a given nanotube is given by the ratio of the number of atoms within a unit cell of the nanotube to the number of atoms within a unit cell of a single sheet of the parent layered material Furthermore, the length of each cutting line is inversely proportional to the length of a unit cell of the nanotube, and the separation between two adjacent cutting lines is $2/d_t$, where d_t is the nanotube diameter [7]. The orientation of the nanotube in the two-dimensional reciprocal space of the parent material is determined by the nanotube chiral symmetry, i.e., the relative orientation of the nanotube axis with respect to the principal axes of the unrolled flat layer of the two-dimensional parent material. Although the zone-folding method is very useful in nanotube science, it experiences certain limitations for small diameter nanotubes, when curvature effects become important due to the hybridization of the electronic in-plane and out-of-plane π orbitals and σ orbitals. The zone-folding method can be applied to the phonons in the same way, as was discussed above for the electrons.

3. Resonance Raman scattering in one-dimension materials

3.1 First-order Raman scattering :

In this section we briefly present the basic ideas of resonance Raman scattering in general emphasizing the main difference among 3D, 2D and 1D systems.

3.1.1. General Formulation

First-order Raman scattering is usually described within the Born–Oppenheimer approximation (the key insight of this approximation is that the motions of the electrons are much faster than that of the ions), and involves quantum mechanical interactions that are treated in third-order time dependent perturbation theory. The Raman scattering process is schematically described by the following events:

   i)   The first electronic transition to an intermediate electron-hole pair state takes place with the annihilation of the incident photon (k_1, ω_1) ;

ii) The second electronic transition to "another" electron-hole pair state occurs with the creation (Stokes) or annihilation (anti-Stokes) of a phonon (q, ω_{ph}) ;

iii) The third transition back to the electronic ground state occurs with an electron-hole recombination process, thus creating the scattered photon (k_2, ω_2).

Processes i) and iii) involve the electron-radiation interaction Hamiltonian (H_{ER}) and process ii) involves the electron-lattice Hamiltonian (H_{EL}) interaction. The conservation of energy and momentum relations

$$\hbar\omega_1 = \hbar\omega_2 \pm \hbar\omega_{ph}$$

$$\hbar k_1 = \hbar k_2 \pm \hbar q_{ph} .$$

are valid in each of i)—iii) processes.

By evaluating the usual expression for the Raman cross-section [8], the Raman intensity is proportional to the square of the Raman matrix element K, which can be written in the form of an integral over energy,

$$|K|^2 = \int \frac{M_f M_f M_0}{(E_1 - E - i\gamma)(E_1 - E \pm E_{ph} - i\gamma)} \rho(E)dE \quad (2)$$

where M_0, M_f and M_f are the transition matrix elements that couple the initial states (0) to the final states (f) through intermediate states (j). In the initial state all N electrons are in the valence band and there are no excited electrons. In quantum mechanical notation, these matrix elements are written as $\langle j'|H_{IR}|0\rangle$, $\langle j|H_{EL}|j'\rangle$, and $\langle f|H_{ER}|j\rangle$, respectively, and $\rho(E)$ in Eq. (2) is the joint density of states (JDOS)[1] that is calculated, taking into account the selection rules for the optical transitions connecting states 0 and j' as well as states j and f, which could typically be states in the valence and conduction bands II. for the moment, we assume that the matrix elements $M_f M_f M_0$ are independent of E, then the quantity K can be calculated by knowing the explicit form of $\rho(E)$. The quantity γ relates to the width or the lifetime of the state under resonance conditions, which can be seen to occur for E in the vicinity of E_1 or the incident photon or in the vicinity of $E_1 \pm E_{ph}$ for the scattered photon. When one of these resonance conditions (with either the incident or scattered photon) is satisfied, the phenomenon is called *Raman scattering*, in contrast to the

situation where E is a virtual state and no resonance process occurs.

However, the matrix elements M_f, M_f and M_0 themselves are dependent on E and on the internal parameters of the system, such as the diameter and chirality of a nanotube or a nanowire, and the direction of the polarization of the light. Of particular importance to Raman scattering are the selection rules introduced by these matrix elements, and these selection rules will in general depend on the physical system under investigation.

3.1.2 The role of dimensionality

Typical joint density of states profiles are obtained from the density of states expression for a single electronic band given in Eq. (1). When Eq. (1) is used to denote the joint density of states, in the case of a direct transition, as in the case of carbon nanotubes, then E_{ii} stands for the electronic transition energy connecting the maximum in the valence band with the minimum in the conduction band. We discuss below the effect of the density of states profile in the *joint density of states* $\rho(E)$ in 1D, 2D and 3D on the Raman intensity

By introducing the joint density of states from Eq. (1) into Eq. (2), the quantity K within the constant matrix element approximation is given by

$$K = M_f M_f M_0 \times \begin{cases} \dfrac{i\pi}{E_{ph}}\left(\dfrac{1}{a} - \dfrac{1}{b}\right) & \text{for } d = 1 \\[2ex] \dfrac{\cdot \ln \cdot}{E_{ph}} & \text{for } d = 2 \\[2ex] \dfrac{i\pi}{E_{ph}}(a - b) & \text{for } d = 3 \end{cases} \quad (3)$$

where d denotes the dimensions of the system, $a = (E_1 - E_f - i\gamma)^{1/2}$ and $b = (E_1 - E_f \pm E_{ph} - i\gamma)^{1/2}$. For a carbon nanotube with light polarized along the tube axis, then the transition energy becomes $E_f = E_{ii}$ and the transition energy is from the ith state in the valence band to the ith state in the conduction band. It is important to observe that for either a 3D, 2D or 1D system, there is an enhancement in K when either $E_1 = E_f$ (resonance with the incident photon) or $E_1 = E_f \pm E_{ph}$ (resonance with the scattered photon) occurs. However, if $\gamma \neq 0$, there is no divergence for the factors in the denominator of K which means that there is no longer a divergence in K for 3D or 2D systems. But for a 1D system, the divergence in K does not only occur in the denominator terms, but in this case a divergence can also occur because of the van Hove singularity in $\rho(E)$. The divergence in the denominators a and b leads to a very strong enhancement in the Raman signal, whenever are sonance occurs either with the incident or scattered light for asystem with any dimensionality. However, for 1D systems there is an additional strong enhancement that

---

1 general the density of states(DOS) is the number of states per unit energy while for the joint density of states (JDOS) the energy unit is placed by an energy difference involved in an optical transition. If the valence and conduction bands are symmetric, the DOS and JDOS are related by a factor of 2, but if they are not symmetric the transition energy under consideration must be considered explicitly.

comes from the singularities in $\rho(E)$ associated with the van Hove singularities, where a large number of states contribute to the resonance scattering over a small energy range. This unique property of the 1D system has allowed the observation of a strong Raman signal from just one carbon nanotube as described in §4, and has allowed the study of not only their phonon properties, but also their structural and electronic properties by the resonance Raman effect, which will be described below. Since there are more possibilities for resonances to occur in 1D systems because of the presence of multiple van Hove singularities in the joint density of states, there are more possibilities that the incident photon excites an electron to the vicinity of a resonant state ($E_{laser} = E_{ii}$), and that after this scattering event, the electron is again scattered to the vicinity of another resonant state E_{jj}. What is meant by the vicinity of a resonant state is discussed in §3.1.3. In the case of resonance with both E_{ii} and E_{jj}, there are two resonant events in the sequence of scattering processes of a single electron and this process is called *double resonance*. Even greater enhancement occurs for the case of double resonance than for the case of ordinary resonance Raman scattering. When such a double resonance sequence occurs, the enhancement can be large enough that the scattering intensity of a higher-order process becomes comparable to a resonant first-order process

For the case of low dimensional systems, the matrix elements will also be modified significantly because of the availability of initial and final states and because the nature of all states (the initial, intermediate and final states) are modified relative to their 3D counterparts.

3.1.3 The Resonance condition for a 1D system

The presence of the cutting lines can have great implications on the Raman scattering in one-dimensional systems, in comparison to Raman scattering in the parent bulk material. The resonance nature of Raman scattering in one-dimensional materials, as discussed below in more detail, can be understood in terms of *cutting lines*. The resonance Raman scattering involves only those electronic states with energies close to the resonance with a given laser excitation energy. In most layered materials, these resonant electronic states, form equi-energy contours around the energy band extrema in two-dimensional reciprocal space. For example, when one goes from a flat sheet of a layered material to a nanotube, the one-dimensional cutting lines are superimposed on the electronic equi-energy contours in two-dimensional reciprocal space, as discussed in §4.1. Thus, the set of resonant electronic states of the one-dimensional nanotube is limited to an intersection of the equi-energy contour with the cutting lines.

We now discuss the implications of cutting lines on resonance Raman scattering in general. Let us consider the intersection of a given cutting line with an equi-energy contour

in more detail. In the vicinity of the electronic energy band edges, such as those associated with infrared (IR) and red laser lines, the equi-energy contours [see Figure 3(a)] can be considered as circles for most layered materials. Three different cases are shown in Figure 5 for the intersection of an equi-energy contour with a cutting line. For the case shown in Figure 5(a), the equi-energy contour is tangential to the cutting line at the point where the contour and the line cross each other. There are a large number of electronic states along the cutting line which are very close to the electronic energy that is resonant with the laser excitation energy, because the direction of the slope of the constant energy contour lies along the cutting line. For each cutting line, there is a specific energy value, such that the equi-energy contour for this energy is tangential to a given cutting line at the point where the contour and the line cross each other. These energy values correspond to the local maxima in the joint density of electronic states (JDOS), and the energy values where the JDOS reaches its local maximum values are called van Hove singularities (VHSs) in the JDOS, as discussed above, but shown from a different point of view in Figure 5. In the case of Raman scattering in one-dimensional systems, when the laser excitation energy E_{laser} matches the energy of the VHS, the light scattering is substantially enhanced due to the high density of electronic states at the VHS.
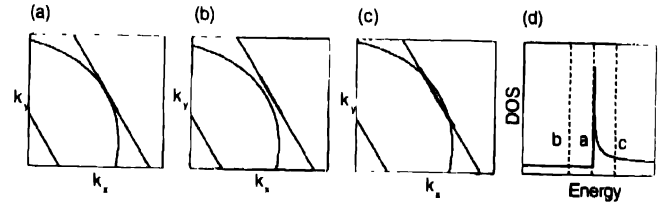
Figure 5. (a) The resonance condition $E_{laser} = E_i$ and two *preresonant* conditions (b) $E_{laser} = E_i - \delta E$ and (c) $E_{laser} = E_i + \delta E$, while (d) the DOS profile of the VHS E_i and the three dashed lines denote the laser energies from (a) to (c), as labeled in the figure (see text for discussion of *preresonant* conditions)

However, the resonance case, as shown in Figure 5(a), is rarely satisfied in practice,and we rather have what is called the *preresonance* condition, where the equi-energy contour is slightly shifted in either direction from the point where it would have been tangential to the cutting line at the cross point of the contour and the line, as in Figure 5(a). The two preresonant cases are shown in Figures (b) and (c), where the equi-energy contour is shifted from the VHS in two opposite directions by an energy δE^2. By comparing Figures 5(b) and (c), one can see that there is a different number of close-lying resonant states, depending on which direction the equi-energy contour is shifted from the VHS, i.e., the JDOS profile of the VHS is asymmetric, decreasing gradually or sharply on the two different sides of the VHS, as shown in Figure(d). When the laser excitation energy increases above the VHS, the number of resonant states decreases gradually [see the bold lines in Figure 5(c)], while for the laser excitation energy decreasing below VHS, there are no resonant states present [see Figure 5(b)]. Note that for both

preresonant cases, there could be substantial contributions to the Raman scattering from the electronic states at or close to the VHS, which are not exactly in resonance with the laser excitation energy, but still can contribute significantly to the Raman signal due to the extremely high DOS at the VHS [see gray lines in Figures. 5(b) and (c)]. While these *preresonant* electronic states are the only states that contribute to Raman scattering in the case when the laser excitation energy is below the VHS [see gray lines in Figure(b)], there are both types of electronic wavevectors, *preresonant* and *resonant*, in the case when the laser excitation energy lies above the VHS [see gray and black bold lines in Figure 5(c)]. The appearance of two different types of wavevectors contributing to the Raman intensity may result in a broadening of the Raman features in the case of the preresonant condition when the laser excitation energy exceeds the VHS.

For clarification, a JDOS profile is shown in Figure 5(d) in the vicinity of the VHS generated by the cutting lines utilized in Figures 5(a) to (c), where the three dashed lines correspond to the three different energies of the equi-energy contours shown in Figures 5(a) to (c), the last two of which show preresonant conditions, and the first shows an exact resonance. We note that the JDOS profile of the VHS is asymmetric, as predicted by analysis of the crossing points between the cutting line and various equi-energy contours. While Figure 5(d) provides a simplified representation of the preresonance conditions pictured in Figures 5 (a) to (c), it loses important information on the distribution of the resonant wavevectors. An analysis of the Raman scattering from a one-dimensional system using the JDOS profile shown in Figure 5 (d) is suitable for rough predictions of the behavior of the Raman features, while a detailed analysis of the Raman features must involve consideration of the resonant wavevectors themselves, and the nature of the resonance (or preresonant) state, shown in Figures 5(a) to (c). For example, when using JDOS profiles, such as the one shown in Figure 5(d), for analysis of the Raman spectra, it must be kept in mind that there could be two different types of preresonant electronic states for case (c) in Figure 5(d), corresponding to black and grey bold lines in Figure 5(c), and these two types of preresonant electronic states correspond to two different dashed lines in Figure 5(d) labeled by (c) and (a), respectively, yet the excitation energy corresponds to the dashed line (c) only.

3.2 Higher-order Raman scattering :

In higher-order Raman scattering processes the wave vectors for an individual phonon can vary from zero to a reciprocal lattice vector, and in the ease of higher-order processes involving more than one phonon, the momentum conservation requirements become

$$k_1 = k_2 + \sum q_i \tag{4}$$

where k_1 and k_2 denote the electron wave vectors in the final and initial states, respectively, and i denotes the various phonons participating in the scattering process. We focus our analysis here, for example, in a two phonon process, whereby the scattering event involves wavevectors q_1 and q_2 such that $q_1 = -q_2$ and $|q_1| = |q_2| = |q|$ in order to fulfill the momentum conservation requirement. If the two phonons belong to the same phonon branch, the phonon energy $(\omega_{ph}(q_1) = \omega_{ph}(q_2) = \omega_{ph}(-q) = \omega_{ph}(q))$. The energy conservation requirement implies that the difference between incident and scattered photons is $\pm 2\omega_q$, being $+$ and $-$ for Stokes and anti-Stokes processes, respectively. It is important to notice that in a second-order scattering process, such as a harmonic process, any wavevectors within the Brillouin zone can contribute to the spectra. The second harmonic of a phonon with any symmetry is expected to have a second harmonic that is Raman-active with A symmetry.

The calculation of the Raman scattering intensity is similar to what was discussed for the one-phonon process in §3.1, except that a matrix element connecting the first and second phonon has to be included in Eq.(3), as well a third term in the denominator. In this process, a very special situation occurs when two resonant terms go to zero simultaneously, thus leading to a *double resonance* process. These double resonance processes are much stronger than single resonance processes in higher-order Raman spectral features. For example, a second-order process obeying double resonance conditions can have an intensity comparable to a single resonance first-order scattering process. Since electrons and phonons are coupled to each other in the resonance scattering process, the double resonance response depends on the electronic structure of the system. A particularly interesting example of this phenomenon occurs in graphite, where a linear dispersion of the electronic states is observed near the Brillouin zone boundary where the valence and conduction bands are degenerate [9, 10]. This special electronic structure combined with the double resonance phenomenon allows us to choose the phonon wave vector by changing the laser energy, and this provides us with a method to probe the phonon dispersion relations of nanometric carbon samples [10] which would be difficult to probe by other currently available techniques. In fact, a number of higher-order modes have been observed in the Raman spectra from carbon nanotubes [11], and are made observable by the double resonance process. Only the simplest and most extensively studied examples are reviewed in this review article.

4. Resonance Raman scattering in one-dimensional prototype materials

Presently there are many known 1D system. Nanowires have been fabricated for many semiconductors, including group IV, III-V, II-VI and IV-VI materials, semimetals such as Bi, Sb, and metals such as Ni, Co, Au, and many others. Nanotubes have been prepared for fewer materials, including carbon, BN, various transition metal chalcogenides, bismuth and phosphorus. In a

few cases, Raman spectra have been taken However. the most detailed Raman spectroscopy studies by far have been carried out on single wall carbon nanotubes (SWNTs). which have become a prototype system for 1D Raman spectroscopy [4]. Furthermore, the carbon nanotube system is sufficiently simple so that detailed calculations can be carried out, and this has indeed been done. It is for these reasons, that this review focuses on the Raman spectra of carbon nanotubes. with particular attention given to the spectra from just one nanotube, where the power of the Raman scattering technique for studying one-dimensional systems is most evident

4.1 Geometrical and electronic structure of carbon nanotubes .

A single wall carbon nanotube can be considered to be a single atomic layer of 2D graphite (called a graphene sheet) rolled up into a seamless cylinder [Figure 6($\mathcal{A}$)]. The structure of each nanotube is uniquely described by two integers (n, m), which refer to the number of a_1 and a_2 unit vectors of the 2D graphene lattice that are contained in the chiral vector. $C_h = na_1 + ma_2$, which spans the circumference of each nanotube [see Figure 6($\mathcal{B}$)] [6]. From the (n, m) indices, the nanotube diameter d_t and chiral angle θ can be obtained from the relations

$$d_t = (a_0 / \pi)(n^2 + nm + m^2)^{1/2} \quad \text{and} \quad \cos\theta = (2n + m) / (n^2 + nm + m^2)^{1/2}$$

In Figure 6($\mathcal{B}$) the vectors a_1 and a_2 denote the unit cell for a 2D graphene sheet. which contains 2 carbon atoms, while the vectors C_h and T denote the much larger unit cell for the nanotube. In general, the diameter of the nanotube is small, and there are only a few (~ 20) carbon atoms around the circumference, with d_t on the order of 1 nm and length on the order of 1 µm, to give a large aspect ratio (length to diameter ratio), thereby yielding a strongly 1D system. The number of carbon atoms within the nanotube unit cell is

$$N = 2(n^2 + m^2 + nm) / d_R$$

where d_R is the greatest common divisor of $(2m + n)$ and $(2n + m)$, and the length of the translation vector T is $\sqrt{3}\pi d_t / d_R$.
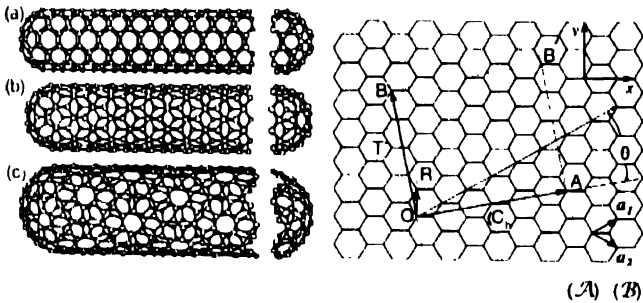
Figure 6. ($\mathcal{A}$) Classification of carbon nanotubes . (a) armchair, (b) zigzag, and (c) chiral nanotubes From the figure it can be seen that the orientation of the six-membered ring in the honeycomb lattice relative to the axis of the nanotube can be taken almost arbitrarily. ($\mathcal{B}$) The unrolled honeycomb lattice of a nanotube When we connect sites O and A, and B and B', a nanotube can be constructed OA and OB define the chiral vector C_h and the translational vector T of the nanotube, respectively The rectangle $OAB'B$ defines the unit cell for the nanotube The vector R denotes a symmetry vector [6].

The reciprocal lattice vectors K_2 along the nanotube axis (continuous) and K_1 along the circumferential direction (quantum confined wavevectors) are obtained from the relation $R_i \cdot K_j = 2\pi\delta_{ij}$, where R_i and K_j are the lattice vectors in real and reciprocal space, respectively [16]. By using the orthogonality relations, we obtain:

$$C_h \cdot K_1 = 2\pi, \quad T \cdot K_1 = 0,$$
$$C_h \cdot K_2 = 0, \quad T \cdot K_2 = 2\pi. \tag{5}$$

K_1 and K_2 can be written as :

$$K_1 = \frac{1}{N}(-t_2 b_1 + t_1 b_2), \quad K_2 = \frac{1}{N}(mb_1 - nb_2), \tag{6}$$

where b_1 and b_2 are the reciprocal lattice unit vectors of a two-dimensional graphene sheet shown in Figure 7 and they are given in (x, y) coordinates by

$$b_1 = \left(\frac{\sqrt{3}}{3}, 1\right)\frac{2\pi}{a}, \quad b_2 = \left(\frac{\sqrt{3}}{3} - 1\right)\frac{2\pi}{a}, \tag{7}$$

while t_1 and t_2 are integers The (n, m) integers appearing in Eq. (6) define the chiral vector C_h. The N wave vectors $\mu K_1 (\mu = 0, ..., N-1)$ giverise to N discrete k vectors in the circumferential direction and they are related to the cutting lines shown in Figure 7.
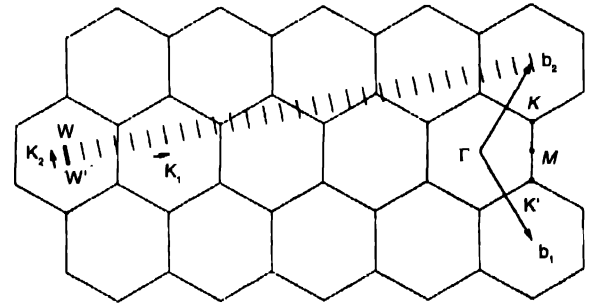
Figure 7. The Brillouin zone of a carbon nanotube is represented by the line segment WW' which is parallel to K_1. The vectors K_1 and K_2 are reciprocal lattice vectors corresponding to C_h and T, respectively The figure corresponds to $C_h = (4,2)$, $T = (4, -5)$, $N = 28$, $K_1 = (5b_1 + 4b_2)/28$, $K_2 = (4b_1 - 2b_2)/28$ [6]

The most remarkable property of carbon nanotubes is that they can be either metallic or semiconducting, depending on their (n, m) indices or chirality. Specifically, the SWNTs for which $(n - m) = 3q$ are metallic,while those for which $(n - m) = 3q \pm 1$ are semiconducting, where q is an integer. The energy band gaps for semiconducting tubes E_{11}^S typically are in the range of several hundred meV and exhibit a $1/d_t$ dependence. Furthermore, the electronic energy band structure and the density of electronic states are also uniquely determined by (n, m) [6, 12, 13]. As discussed in §3, the singularities in the density of states are called van Hove singularities (VHS), and

they appear prominently as sharp peaks in the density of states, as shown in general in Figure 4, and for three specific (n, m) single wall metallic nanotubes in Figure 8(a).
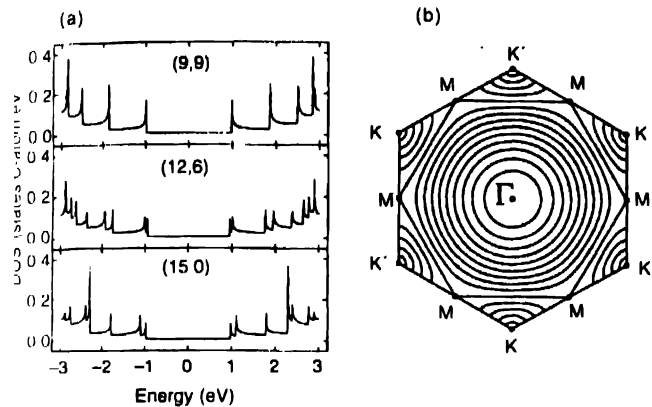
(a)   **(b)**

Energy (eV)

Figure 8. (a) The 1D electronic density of states for the valence and conduction bands vs energy (the Fermi level is at $E = 0$) for three metallic nanotubes of approximately the same diameter, showing the effect of chirality and trigonal warping (see text) on the van Hove singularities in the density of states (9,9) (armchair), (12,6) (chiral), and (15,0) (zigzag) with diameters 1.22 1.24 and 1.17nm, respectively The plots are made the tight binding approximation, assuming that the energy overlap integral is $\gamma_0 = 2.9$ eV and the wave function overlap integral vanishes; - 0 [6] (b) Plot of the 2D equi-energy contours of 2D graphite, showing trigonal warping effects in the contours, as we move from the K point in the $K - \Gamma$ or $K - M$ directions The equi-energy contours are circles near the K point and near the center of the Brillouin zone Γ, but near the M points on the zone boundary, the contours are straight lines which connect the nearest M points [7]

4 2 Raman spectra from one isolated nanotube :

The resonance Raman effect occurs when the energy of the incident or scattered photon is in resonance with an inter band transition from the valence band state i to a conduction band state f for light polarized along the nanotube axis $(\hat{z})$ [14, 15].

Since the resonance enhancement for a 1D system is very high, it is possible to see Raman spectra from one isolated single wall carbon nanotube.

Figure 9 shows typical Raman spectra from a single isolated semiconducting and a metallic single wall carbon nanotube on a Si/SiO$_2$ substrate. The four most important features seen in Figure 9 are the radial breathing mode (RBM) where the carbon atoms are all vibrating in phase in an A symmetry mode in the radial direction of the nanotube (see left inset to Figure 9 to view the atomic displacements associated with the radial breathing mode), the tangential G-band which is derived from the in-plane Raman-active mode in graphite (see right inset to Figure 9 to view the longitudinal and transverse displacements for the G-band with A symmetry), the disorder-induced D-band, and its second-order harmonic (the G-band). It is significant that the Raman signal from one nanotube, ~ 1 nm in diameter, is of comparable intensity to the signal from the silicon atoms, which are approximately 10^6 times more numerous within the laser spot size of ~ 1 μm, as can be seen in Figure 9 [16].

The Raman spectra in Figure 9 at the single nanotube level provide two important pieces of information. The first relates to the *diameter selective* aspect of the spectra, and the second relates to distinguishing between *semiconducting* and *metallic* nanotubes. [4, 16]. Referring to Figure 8(a) we see the density of states of the conduction band for three *metallic* (M) carbon nanotubes, all withabout the same diameter. Within the simplest model for the electronic structure where the overlap integral within the tight binding model vanishes $(i.e., s = 0)$ [6], the density of the states for the valence band is the mirror image of that for the conduction bands [Figure 8(a)]. Since the energy separation for the lowest energy inter band transition E_{11}^M, from the highest valence VHS to the lowest conduction band VHS, varies inversely as the tube diameter, the resonance condition depends

RBM   **G-band**
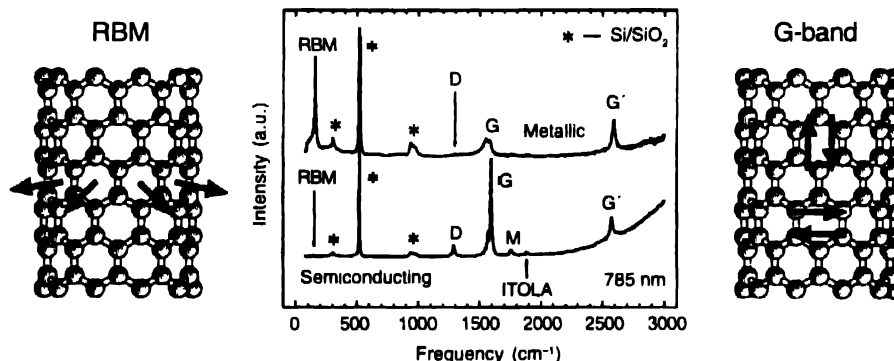

Frequency (cm⁻¹)

Figure 9. Raman spectra from a metallic (top) and a semiconducting (bottom) SWNT at the single nanotube level using 785 nm (1 58 eV) laser excitation, showing the radial breathing mode (RBM, D-band, G-band and G' band) features in addition to weak double resonance features associated with the M-band and the iTOLA feature (see §4.9 [11]. The mode on the left and the right show, respectively, the mode displacements associated with the RBM and G-band normal mode vibrations. The vibrations along the nanotube axis are denoted by G^+ and the vibrations in the circumferential direction are denoted by G^-, because the G^- modes downshift in frequency relative to the G^+ modes because of the nanotube curvature effect. The isolated carbon nanotubes are sitting on an oxidized silicon substrate which provides contributions to the Raman spectra denoted by '*' that are used for calibration purposes as described below [17].

on the nanotube diameter. Furthermore, since the radial breathing mode frequency for an isolated nanotube varies as $\omega_{RBM} = \alpha / d_t$, the diameter of a nanotube in resonance with a given laser excitation energy E_{laser} can be determined experimentally by the Raman effect. For an isolated SWNT sitting on a Si/SiO$_2$ substrate, the constant α has been determined to be 248 cm^{-1}nm [16]. Because of this diameter selective effect [18], study of the radial breathing mode frequencies for various E_{laser} values can be used for characterizing the diameter distribution of SWNTs in a sample of SWNT bundles [19]. Inspection of the two spectra in Figure 9 indicates a distinctly different G-band lineshape, which can be used to distinguish metallic from semiconducting nanotubes

4 3 Determining the geometrical structure of a nanotube by Raman scattering .

Since the electronic energy bands of 2D graphite do not show simple circular constant energy contours, in Figure 8(b), but rather show a trigonal warping effect [6, 7], there is a weak dependence of the electronic energy levels of single wall carbon nanotubes (SWNTs) on chiral angle θ, as well as a much stronger dependence on nanotube diameter d_t, which determines the number of carbon atoms in the circular cross-section of the nanotube shell one atom in thickness [6].

The weak dependence of the electronic energy bands of SWNTs on chiral angle θ relates to the 3-fold symmetry of the electronic dispersion relations about the K-point of the 2D graphene Brillouin zone [see Figure 8(b)], where the graphene valence and conduction bands are degenerate, forming a zero band gap semiconductor [6]. This trigonal warping effect in Figure 8(b) is responsible for each (n, m) SWNT having a unique spectrum of singularities in the density of states of their conduction and valence bands, when the energy bands of the 2D graphene lattice are zone folded to form the energy bands of the SWNTs [6, 7]. This chirality dependence of the van Hove singularities [7, 20] in the 1D electronic density of states (DOS) of the conduction band, is demonstrated in Figure 8(a) for three metallic (n, m) nanotubes, all having about the same diameter d_t (from 1 17 nm to 1.24 nm), but having different chiral angles: $\theta = 0^\circ$ (zigzag), 10.16° (chiral), and 30.0° (armchair) for nanotubes (15,0), (12,6), and (9,9), and diameters of 1.17, 1.24 and 1 22 nm, respectively. The plot shows that as the chiral angle is varied from the armchair nanotube (9,9) ($\theta = 30^\circ$) to the zigzag nanotube (15,0) ($\theta = 0^\circ$), a splitting due to trigonal warping effects [see Figure 8(b)] develops in all of the singularities in the DOS [7, 20], and this splitting increases in magnitude with decreasing chiral angle. Since the peak energies in the density of states [see Figure 8(a)] are unique for each (n, m) value, the interband transition energies E_{ii} between valence bandstate i and conduction band state i are also unique, where $i = 1,2, ...$

and the superscript index M or S is added to denote metallic or semiconducting tubes. For carbon nanotubes, interband transitions are strongly favored when the photon energy excites an electron from the ith peak in the valence band density of electronic states to the ith peak in the conduction band density of states[3]. These would correspond to vertical transitions in the extended zone (2D graphene). This energy is denoted by E_{ii}, which is called the peak energy or van Hove singularity in the joint density of states, giving rise to a *unique* set of singularities in the joint density of states (JDOS) E_{ii} for each (n, m) value. A plot of the singularities in the JDOS denoted by E_{ii} is presented in Figure 10 as a function of nanotube diameter d_t [21]. Reliable values of E_{ii} are obtained by the tight binding approximation for $d_t > 0.9$ nm

As can be seen in Figure 10, the trigonal warping effect [Figure 8(b)] causes a spread of the interband energies E_{ii} between the singularities in the joint density of states (JDOS), for nanotubes with the same diameter d_t. Here the integer i denotes the singularities in the JDOS as the energy relative to the Fermi level E_F increases. From the above discussion, we conclude that each nanotube (n, m) has a unique set of interband energies E_{ii}, denoting the energy differences between the ith van Hove singularities in the conduction and valence bands And, conversely, if one interband energy E_{ii} and a nanotube diameter d_t are specified, then its corresponding unique (n, m) can in general be identified
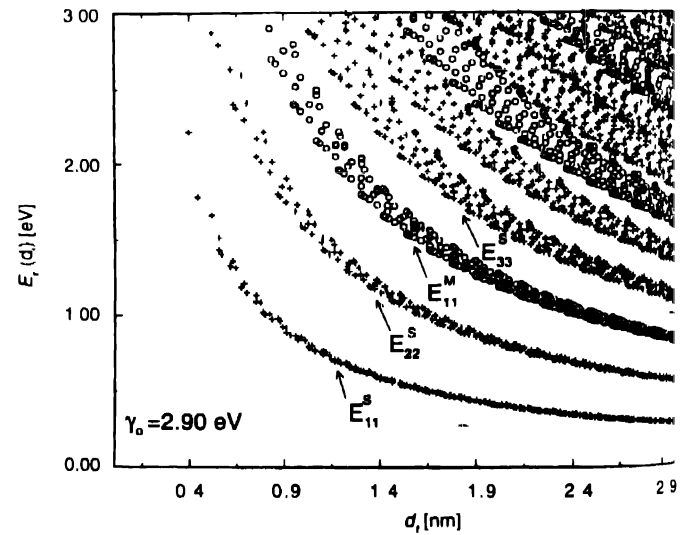
Figure 10. Calculated energy separations E_{ii} between van Hove singularities i in the 1D electronic density of states of the conduction and valence bands for all (n,m) values vs nanotube diameter $0.4 < d_t < 3.0$ nm, using a value for the carbon-carbon energy overlap integral of $\gamma_0 = 2.9$ eV and a nearest neighbor carbon-carbon distance $a_{c-c} = 1.42$Å [7, 22] Semiconducting (S) and metallic (M) nanotubes are indicated by crosses and open circles, respectively The index i in the interband transitions E_{ii} denotes the transition between the van Hove singularities, with $i = 1$ being closest to the Fermi level taken at $E = 0$ [7, 21, 22].

This fact leads to what is special about the resonance Raman effect in this 1D system, and this is the information about the geometrical structure of the nanotube that is provided by

sonance Raman spectra at the single nanotube level. Normally ie resonance Raman effect just gives *spectral* information, or information about phonon frequencies, electronic energy levels nd the electron-phonon interaction, but *not structural* information directly. But in the resonance Raman process for its 1D system, every (*n, m*) nanotube can be considered as a ifferent molecule, and is in resonance with a unique set of iterband energies E_{ii} (*n,m*), as shown in Figure 8(a) and 10, so iat for this 1D system, resonance Raman spectra can also ield structural information through identification of the (*n,m*) alues that correspond to the observed Raman spectra for a iven isolated SWNT. Once (*n,m*) is known from measurements iade on the radial breathing mode feature, Raman studies on solated carbon nanotubes can be carried out to understand ietail the dependence of *all* the features shown in the spectrum [Figure 9 on diameter d_t, chiral angle θ, laser excitation energy E_{laser}, and other pertinent parameters. Furthermore, the spectra bserved for these other features in Figure 9 are also sensitive id and θ and canbe used to corroborate the (*n, m*) assignments.

Resonance Raman characterization of the (*n, m*) indices for ne nanotube is important for scientific studies of SWNTs, nsofar as many physical properties, such as transport, optical, nechanical,and other properties, that depend sensitively on the *n, m*) indices [6], can be studied systematically at the single ianotube level through use of the resonance Raman effect to dentify their (*n, m*) values.

The determination of (*n, m*) by resonance Raman scattering lepends on the determination of both E_{ii} and d_t by exploiting he unique relation between E_{ii} and (*n, m*) shown in Figure 8(a), ind the direct determination of d_t from the radial breathing mode relation $\omega_{RBM} = 248/d_t$, as discussed above. The Ietermination of E_{ii} is carried out most conveniently and iensitively by measurement of the radial breathing mode feature, hough other features (such as the *G*-band, *D*-bandand *G'*-band) in the resonance Raman spectrum (see Figure 9) are often used to confirm the (*n, m*) assignment made from analysis of the RBM ipectrum. If a tunable laser were available to be tuned to E_{ii} (which could be detected as the E_{laser} value where the maximum intensity in the Raman spectrum occurs), then a simple measurement of ω_{RBM} to yield d_t and to identify the index *i* in E_{ii} (see Figure 10) would be sufficient to determine (*n, m*). In practice, such a tunable laser system has thus far only been applied to single nanotube Raman spectroscopy studies over a small energy range (~0.15 eV) for only one SWNT [17], and this is in part due to the fact that only a few laboratories world wide ave available tunable laser systems working over a broad energy inge in conjunction with a Raman micro-probe system.

Nevertheless, an (*n, m*) determination can in most cases be nade if a nanotube is within the resonant window of a single vailable laser excitation line, which in practice is satisfied for E_{laser} within ~ ± 0.1 eV of an interband transition for that ianotube. If only a single laser line is available, then the E_{ii} is

determined from its relative intensity in relation to how well the nanotube is in resonance with E_{laser} (see §3.1.3)), making use of the tight binding determination of the E_{ii} values for (*n, m*) SWNTs within the resonance window [16].

One method to determine E_{ii} directly requires measurement of both the Stokes and anti-Stokes radial breathing mode spectra [23, 24], and this is discussed in § 4.4 in terms of the availabity of a single laser excitation line, but the availability of a tunable laser for the measuremnt of the anti-Stokes/Stokes intensities substantially increases the accuracy in the determination of the E_{ii} value, as discussed in §4.5.Thus, through the quantum confinement effect in a 1D system, the appearance of sharp singularities in the density of states, and the fact that each nanotube can be considered as a distinct molecule with a unique structure specified by its (*n, m*) indices and with a distinct set of van Hove singularities where the resonance Raman effect provides the greatest enhancement to the Raman signal, it is possible to use resonance Raman scattering as a sensitive probe of the geometric structure of a 1D system.

4.4 Tunable Laser Spectroscopy :

The resonance Raman intensity is proportional to the joint density of electronic states (JDOS) in the sample and, therefore, resonance Raman scattering (RRS) measurements made with a tunable laser provide a highly reliable technique to study the JDOS of isolated SWNTs, and consequently the profile of the DOS can be determined. Thus RRS can be used to determine the energy value for the one-dimensional van Hove singularities of a SWNT with a precision better than 5 meV, thereby providing important information that could be used for subsequent measurements on the same SWNT. As we see below, with RRS, the measured width of the JDOS is on the order of ~ 0.1 – 1.0 meV, further demonstrating that SWNTs really provide a remarkably good model for 1D mesoscopic systems. This result can be compared with the DOS obtained, for example, by scanning tunneling spectroscopy. RRS has an advantage over techniques such as scanning tunneling spectroscopy (STS), since RRS useslight to probe the DOS of SWNTs and is not expected to significantly perturb their 1D electronic structure, as does STS which is a much more strongly interacting probe. The observation of a measurable Raman signal from one SWNT suggests that the intrinsic van Hove singularities in SWNTs must be much sharper than were observed in STS experiments [25,26].

Due to the quantum confinement of the DOS, strong resonant effects occur in the Raman scattering from an isolated SWNT when the energy of the incident or scattered light matches an electronic transition E_{ii} between van Hove singularities in the valence and conduction bands, thereby strongly enhancing the Raman signal [25, 26].

Figure 11 shows an atomic force microscopy (AFM) image of the substrate with lithographic markers on an 8 × 8 µm² lattice. The light spot (~ 1 µm diameter) is located close to the marker (~

I μm size) in order to achieve good precision in always returning the light spot to the same position on the substrate as the laser energy E_{laser} is changed. The dashed circle in Figure 11 displays the position where the laser spot is placed, showing the presence


Figure 11. AFM image of the sample The left image shows the markers used to localize the spot position (dashed circle) on the substrate during the Raman experiment, and for further AFM characterization of the SWNTs present within the light spot (right image) [17]

of some isolated SWNTs (see right AFM image of Figure 11). The excitation was provided by a tunable Ti:Sapphire laser (power level $P < 10$ mW on the sample) pumped by an Ar ion laser (6W) The incident light was filtered with a single-monochromator (McPherson - 1200g/mm), and the scattered light was analyzed with an XY DILOR triple-monochromator equipped with a N_2 cooled CCD detector. Raman spectra of the sample were measured in the laser excitation range 720 nm (1.722 eV) $\leq E_{laser} \leq 785$ nm (1.585 eV) with steps of 4 nm (~0.009 eV) All the Stokes and anti-Stokes spectra were corrected to account for spectrometer efficiency at each laser energy, and the spectra were then normalized by the 303 cm^{-1} Si substrate peak intensities. The anti-Stokes intensities were multiplied by $\{[n(\omega)+1]/n(\omega)\}$, where $n(\omega) = 1/[\exp(\hbar\omega/k_B T)-1]$ is the Bose—Einstein thermal factor, ω is the phonon frequency, k_B is the Boltzmann constant, and T is the temperature. Although high laser power was used to measure the Raman spectra, T was found to be close to room temperature (not higher than 325 K), and this was confirmed by changing the laser power from 1 mW/μm^2 (10 MW/cm^2) to 10 mW/μm^2 (100 MW/cm^2), where the Stokes/anti-Stokes intensity ratio for the 521 cm^{-1} and 303 cm^{-}

^{1} Si peaks remained constant, the ω_{RBM} peak for the nanotube did not show a temperature-dependent shift, and the intensity ratios between the RBM features, and the 303 cm^{-1} Si peaks also remained constant, in both the Stokes and anti-Stokes spectra. The gold marker near the light spot, however, probably experienced some heating.

With the light spot position shown in Figure 11, the Raman spectra were measured with different laser excitation energies. Figure 12 shows the Stokes and anti-Stokes Raman spectra of one light spot for several different excitation laser energies, with E_{laser}, increasing from the bottom to the top spectra (see caption). From Figure 12, the RBM feature at 173.6 cm^{-1} appears and

disappears over the tunable energy range of E_{laser}, thereby allowing us to tune over the whole resonant window of one van Hove singularity in the JDOS of this resonant SWNT. The linewidth for this $\omega_{RBM} = 173.6$ cm^{-1} peak is 5 cm^{-1}, typical of that of one isolated SWNT [30]. The points in Figure 13 show the peak intensity of the 173.6 cm^{-1} RBM feature vs. E_{laser} in the Stokes and anti-Stokes processes. As discussed in the
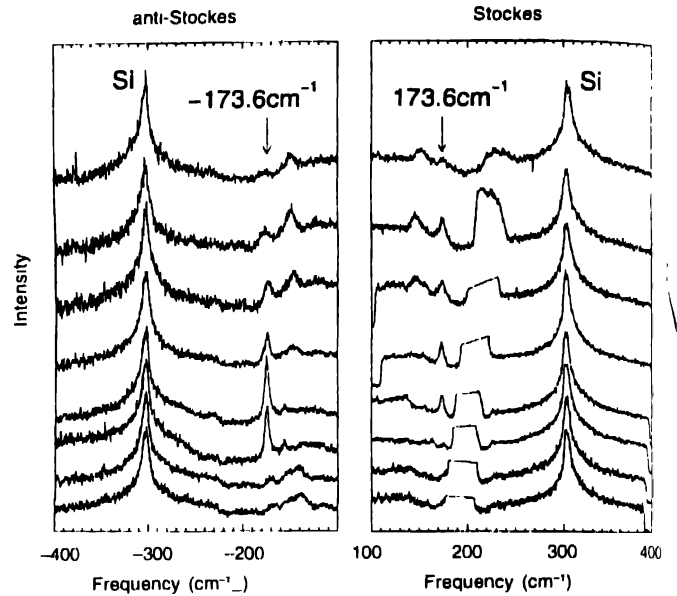
Figure 12. Stokes and anti-Stokes Raman spectra from isolated SWNTs on a Si/SiO₂ substrate for several different laser excitation energies From bottom to top, the spectra were taken at laser energies $E_{laser} = 1.621$, 1.631, 1.640, 1.649, 1.666, 1.685, 1.703, and 1.722 eV The flat region appearing in all Stokes spectra comes from light leakage, and was cut out from the spectra [17]
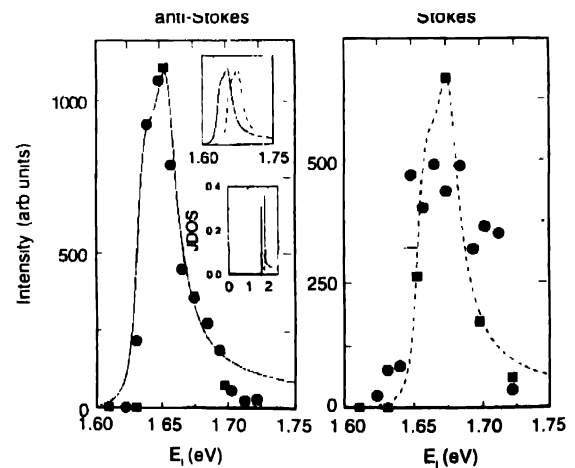
Figure 13. Raman intensity vs laser excitation energy E_{laser} for the $\omega_{RBM} = 173.6$ cm^{-1} peak in the Stokes and anti-Stokes Raman processes Circles and squares indicate two different E_{laser} runs on the same SWNT sample The line curves indicate the resonant Raman window predicted from Eqs (8) and (9), with $E_{ii} = 1.655$ eV, $\Gamma_r = 8$ meV, and $\Gamma_J = 0.5$ meV. The upper inset compares the theoretically predicted Stokes and anti-Stokes resonant windows The lower inset plots the JDOS for one isolated (18,0) SWNT with $\Gamma_J = 0.5$ meV for all van Hove singularities up to 2.5 eV[17]

beginning of this section, these resonant windows reflect the JDOS of the resonant SWNT.

Figure [13] shows that the resonant window in the anti-Stokes process is clearly asymmetric, exhibiting, from lower to higher E_{laser}, a very sharp increase in signal, followed by a slower decrease. The Stokes signal quality is not as good as the anti-Stokes signal due to the frequency dependent spectrometer efficiency that drops off rapidly with increasing laser wavelength, being worse in the Stokes frequency region. However, a similar E_{laser} dependent behavior is observed for both resonant windows (see Figure 13). This asymmetric behavior is caused by the asymmetry in the JDOS $\rho(E)$ of one isolated SWNT. The RBM peak intensity $I(E_{laser})$, which is a function of E_{laser}, can be evaluated from $\rho(E)$ according to

$$I(E_{laser}) = $$

$$\frac{M}{(E_{laser} - E - i\Gamma_i)(E_{laser} \pm E_{ph} - E - i\Gamma_r)} \rho(E) \, dE \quad (8)$$

where the first and second factors in the denominator, respectively, describe the resonance effect with the incident and scattered light, where the + (–) applies to the anti-Stokes (Stokes) process for the phonon of energy E_{ph}, and Γ_r gives the inverse lifetime for the resonant scattering process. Here $M = M_i M_i M_0$ is considered to be independent of E in this small energy range, where M_0, M_i and M_j are, respectively, the matrix elements for the electron-radiation absorption, the electron-radiation emission, and the electron-phonon interaction.

For one isolated SWNT, the detailed JDOS profile must be taken into account, and $\rho(E)$ can be expressed by

$$\rho(E) = Re\left[\sum_i d_i \gamma_0 \frac{a_{C-C} E}{\sqrt{(E - E_{ii} - i\Gamma_j)(E + E_{ii} + i\Gamma_j)}}\right] \quad (9)$$

where a_{C-C} is the nearest-neighbor distance between carbon atoms, γ_0 is the tight binding overlap integral, and Γ_j is introduced as a measure of the finite nanotube size effect on the width of the JDOS singularity for the E_{ii} electronic transition. The sum over i takes into account the different van Hove singularities of one SWNT.

The line curves in Figure 13 show plots for the Stokes (dashed line) and anti-Stokes (solid line) resonant windows, using Eqs. (8) and (9) and $E_{ph} = 21.5$ meV obtained from $\omega_{RBM} = 173.6$, cm^{-1}. The width of the resonant windows gives $\Gamma_i = 8$ meV The fit between the experimental points and Eqs. (8) and (9) yields $E_{ii} = 1.655 \pm 0.003$ eV and Γ_j in the range of ~0.1–1.0 meV, which is much smaller than the widths for the DOS features observed by STS (~ 30 meV) [25, 26], and accounts for the observed asymmetry in the resonant window of one SWNT.

The upper inset shows a comparison between the theoretically predicted Stokes and anti-Stokes resonant windows, revealing a shift in these resonant windows due to the resonant condition for the scattered photon, $E_s = E_{ii} \pm E_{ph}$ for the anti-Stokes (+) and the Stokes (–) processes.

From theory, taking $\gamma_0 = 2.90$ eV, $a_{C-C} = 0.142$ nm, and $\alpha = 248$ cm^{-1} nm in the relation $\omega_{RBM} = \alpha/d_t$ [16], we have very few possibilities for SWNT indices (n, m) which satisfy the observed $E_{ii} \sim 1.655$ eV and $\omega_{RBM} \sim 173.6$ cm^{-1}. The best candidates are metallic SWNTs with an E_{11}^M that is split by the trigonal warping effect [7]. Three candidates were considered in the identification : indices (12,9) have $d_t = 1.45$ nm, $E_{11}^M = 1.684$ eV and 1.725 eV, and $\omega_{RBM} = 171.2$ cm^{-1}; indices (17,2) have $d_t = 1.44$ nm, $E_{11}^M = 1.650$ eV and 1.817 eV, and $\omega_{RBM} = 172.7$ cm^{-1}; while indices (18,0) have $d_t = 1.43$ nm, $E_{11}^M = 1.655$ eV and 1.831 eV, and $\omega_{RBM} = 173.5$ cm^{-1}. The best fit was obtained by identifying the signal as coming from a (18,0) SWNT. The experimental value at $E_{ii} = 1.655$ eV is in very good agreement with the E_{11}^M predicted for the (18,0) SWNT based on tight-binding calculations [6]. The second van Hove singularity predicted at 1.831 eV was not observed because the laser could not be tuned above 1.722 eV. Inside the dashed circle in the right image of Figure 11, there is one SWNT (with $d_t = 1.5 \pm 0.2$ nm) which is a good candidate for the resonant (18,0) SWNT.

Finally, the lower inset to Figure 13 plots the highly singular JDOS vs. E_{laser} for one isolated (18,0) SWNT obtained from Eq. (9) and considering the experimental value $\Gamma_j = 0.5$ meV taken for all van Hove singularities, since Γ_j is related to finite size effects for each SWNT.

In summary, by using a tunable laser, it is possible to study the JDOS profile $\rho(E)$ of one isolated SWNT, giving the singular E_{ii} value with a precision better than 5 meV. The value obtained for $\Gamma_j \sim 0.1 - 1.0$ meV is considerably smaller than the values obtained with STS [25, 26] suggesting that the DOS in SWNTs exhibits strong 1D behavior. Therefore, resonance Raman spectroscopy can be used to characterize the JDOS of an isolated SWNT, thereby providing important information that could be subsequently used for other properties measurements on this characterized SWNT.

4.5 Stokes/anti-stokes asymmetries :

In the non-resonance Raman spectra, the anti-Stokes to Stokes intensity ratio for a Raman line is used to determine the temperature of the sample through the relation

$$I_{AS}/I_S = \exp\left(-E_{ph}/k_B T\right) \quad (10)$$

In the case of resonance Raman scattering for a 1D system, this approach for determining the temperature of a system cannot be carried out because the I_{AS}/I_S ratio does not depend only on

the thermal population factor, but also depends on the resonant contribution from the scattered photons that has different energies for the Stokes $(E_{laser} - E_{ph})$ and anti-Stokes $(E_{laser} + E_{ph})$ processes. This effect is a consequence of the displacement of the Stokes and anti-Stokes resonance windows, as discussed in §4.4, where a tunable laser is used. Special 1D aspects of the density of electronic states are obtained by measuring the Stokes and anti-Stokes spectra of carbon nanotubes in both single wall nanotube bundles and isolated carbon nanotubes. The information provided by study of both the Stokes and anti-Stokes spectra in SWNT bundles includes the observation of resonance Raman scattering profiles to which only metallic nanotubes contribute (Stokes spectra), and other scattering profiles to which only semiconducting nanotubes contribute (anti-Stokes). This is unique to the resonance Raman spectra of carbon nanotubes, and reveals their 1D character, whereby in one process the laser is in resonance with a metallic 1D system, while in the other process a 1D semiconducting system is being probed [29]

In the case of isolated nanotubes, the information provided by the anti-Stokes and Stokes spectra is even richer. Because of different resonant denominators in the Raman intensity [see Eq (10)], the I_{AS}/I_S ratio is sensitive to the laser excitation energy E_{laser} and this sensitivity can be used to measure the energy of the quantized electronic state E_{ii} [23]. One-dimensional systems, such as carbon nanotubes, are suitable for illustrating this concept because the resonance is very sharp in energy and large asymmetries between the anti-Stokes and Stokes intensities can be observed, as shown in Figure 14 (a) and (b) The radial breathing modes for these two nanotubes yield d_t values that are very close to one another, so that it is not possible to

distinguish one nanotube from another from the measured d_t values. However, the ratio of the anti-Stokes to Stokes intensities, is very different for the two nanotubes, and this large asymmetry in I_{AS}/I_S is then used to sensitively determine the energy E_{ii} of the resonant van Hove singularity in the joint density of states (right hand panels in Figure 14). This determination is done by calculating the experimental $E_{ii}^{exp'}$ that would produce the measured I_{AS}/I_S ratio. By using this approach, the nanotube geometry (n, m) is determined as the best fit of the measured d_t and $E_{ii}^{exp'}$ to the predicted d_t and E_{ii} values for a given (n, m), thereby providing a precise experimental determination of the (n, m) indices. This is illustrated in Figure 14 for the (n, m) nanotubes $(12, 1)$ and $(11, 3)$, which have very similar d_t values, but very different experimental E_{22}^S values of 1.587 and 1.554 eV, respectively [23]. These experimental values for E_{22}^S are to be compared to their corresponding theoretical values of 1.585 and 1.564 eV, obtained on the basis of tight binding calculations [6].

Based on the anti-Stokes to Stokes asymmetries, we can predict the situation whereby the I_{AS}/I_S is equal to one. In this case, only the resonant denominator term that contains the resonance with the incident photon is contributing to the total intensity and both anti-Stokes and Stokes are equally enhanced. This special situation occurs when the laser excitation energy is very close to E_{ii}. Such a situation is observed for the nanotube depicted in Figure 15. In these spectra we see that the RBM intensities are very large compared to the feature from the silicon substrate at 303 cm^{-1}, because of the strong resonance condition, i.e., close to the case (a) in Figure 5. In this section, we have illustrated by showing some examples of the Stokes and anti-Stokes spectra for the radial breathing mode of carbon

(a)   (b)
                    (12,1)   (11,3)
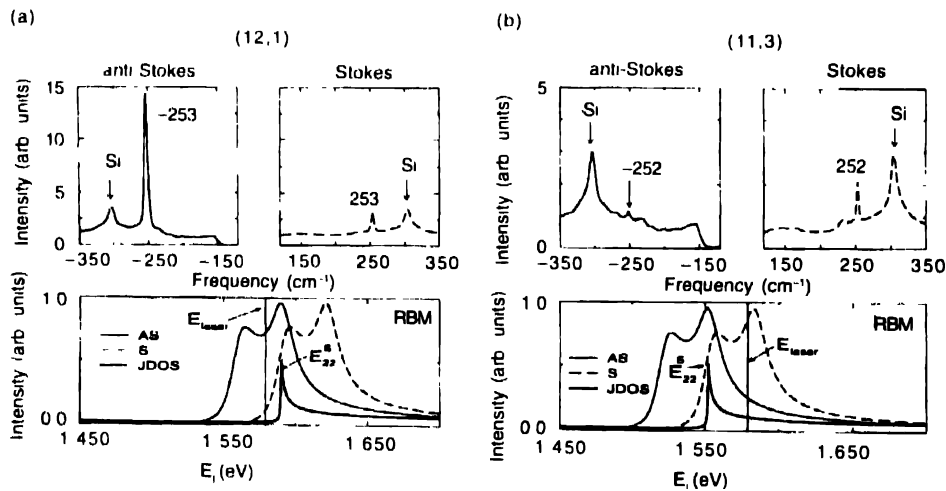
Figure 14. Resonance anti-Stokes (AS) and Stokes (S) spectra for a (12,1) semiconducting SWNT on a Si/SiO$_2$ substrate using 1 579 eV (785 nm) laser excitation (upper panels) and the predicted joint density of states (heavy line) and resonance windows for the RBM mode in the anti-Stokes (solid line) and Stokes (dashed line) processes for the (12,1) SWNT (lower panel). (b) is the same as in (a), except that the data are for the (11,3) SWNT. The energy E_{22}^S in (a) and (b)in the lower panels is varied to obtain the experimentally measured I_{AS}/I_S ratio at E_{laser} =1.579 eV given in the upper panels of (a) and (b), where the AS spectra are normalized by the Boltzmann factor for easy comparisons of the relative AS and S intensities. In the lower panels the laser line at E_{laser} = 1 579 eV is denoted by a solid vertical line [23]

nanotubes how the special 1D electronic structure allows the resonant Raman effect to measure the critical points in the density of electronic states to an accuracy of ~ 10 meV using one laser line, and to an accuracy of 5 meV using a tunable laser (see §4.4). It is expected that this kind of approach could also be applied to other low-dimensional systems in order to determine the energy of the confined states by using light scattering.
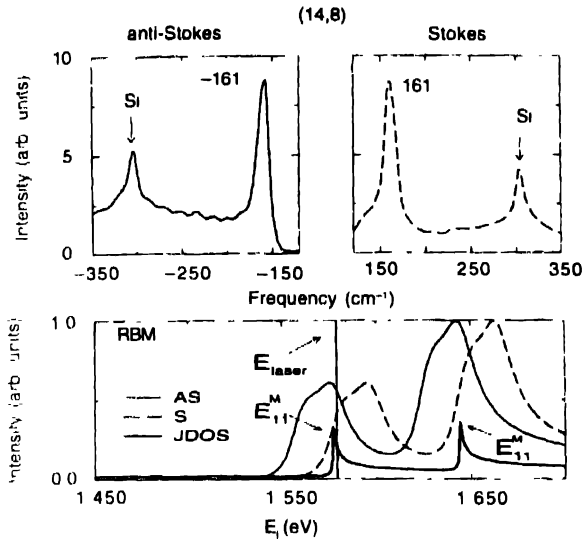

(14,8)

Figure 15. (a) Resonance anti-Stokes (AS) and Stokes (S) spectra for a (11,8) metallic SWNT on a Si/SiO₂ substrate using 1.579 eV (785 nm) laser excitation (upper panels), and the *predicted* joint density of states (heavy line) and resonant windows for the RBM mode in the anti-Stokes (solid line) and Stokes (dashed line) processes for the (14,8) SWNT (lower panel). The two van Hove singularities labeled E_{11}^M for the (14,8) SWNT, split by the trigonal warping effect, are indicated on the Figure [23].

1.6 G-band lineshape Dependence on the Resonance Condition :

In §4-5 we discussed the introduction of asymmetries into the Stokes and anti-Stokes intensities by the resonance conditions for the scattered photon, thus giving rise to departures from the usual Bose–Einstein thermal relation [Eq. (10)]. However, this difference in resonance conditions for the scattered photon, not only causes Stokes vs. anti-Stokes asymmetry, but it can also cause changes in the lineshape of a Stokes Raman feature composed of different phonon constituents.

Strong resonance occurs when the incident or scattered photon energy matches an actual electronic transition between van Hove singularities in the 1D material. Resonance with the incident photon enhances the Raman cross section related to all phonons in the 1D material by the same amount. However, resonance with the scattered photon can enhance different Stokes Raman peaks by different amounts. Since the scattered photon energy depends on the phonon energy, different amounts of resonance enhancement occur for phonons with different energies. Similar to the case of the Stokes/anti-Stokes intensity ratio(§4.5), where the scattered photons have different

energies $\hbar\omega_i - \hbar\omega_{ph}$ as compared to $\hbar\omega_i + \hbar\omega_{ph}$, a Stokes Raman process involving two phonons ω_{ph1} and ω_{ph2} with different energies will exhibit scattered photons with different frequencies $\hbar\omega_i - \hbar\omega_{ph1}$ and $\hbar\omega_i - \hbar\omega_{ph2}$. Therefore, the relative intensities between the Raman peaks in the Stokes Raman spectra will depend on the resonance condition, namely how close these photon energies are to the 1D van Hove singularities E_{ii}. The observation of this effect is discussed below for the G-band Raman feature in SWNTs.

The G band is a complex SWNT spectral feature. Due to the folding of the graphite Brillouin zone into the SWNT zone, and due to the symmetry-breaking effects associated with the nanotube curvature, the E_{2g} peak in the Raman spectra of graphite splits into several modes with different symmetries in the Raman spectra of SWNTs [31, 32]. Six modes [two $A(A_{1g})$, two $E_1(E_{1g})$ and two $E_2(E_{2g})$] are both predicted and observed to be Raman active in the G band of SWNTs [6, 33-40]. Symmetry assignments of the different phonon modes in *semiconducting* SWNTs were determined by polarized Raman experiments performed on a bundle of aligned SWNTs ($d_t = 1.85 \pm 0.25$ nm) using an excitation laser energy $E_{laser} = 2.41$ eV [35]. The G-band profile for semiconducting SWNTs in the SWNT bundle was deconvolved into four spectrally resolved SWNT components with the following symmetry assignments :

$\omega_G^- \sim 1549$ cm$^{-1}[E_2(E_{2g})]$, $\omega_G^- \sim 1567$ cm$^{-1}[A(A_{1g}) + E_1(E_{1g})]$, $\omega_G^+ \sim 1590$ cm$^{-1}[A(A_{1g}) + E_1(E_{1g})]$, and $\omega_G^+ \sim 1607$ cm$^{-1}[E_2(E_{2g})]$. [35] For metallic SWNTs, the G-band profile is quite different due to plasmon-phonon coupling, and we focus our discussion on the more simple G-band spectra of semiconducting SWNTs.

The intensity ratio between the two most intense features denoted by ω_G^- and ω_G^+ and corresponding to the lower and upper frequency components, is in the range $0.1 < I_{\omega_G^-}/I_{\omega_G^+} < 0.3$ for most isolated semiconducting SWNTs (~ 90%) that have thus far been studied [41]. However, unusually high or low $I_{\omega_G^-}/I_{\omega_G^+}$ ratios have been observed for a few spectra coming from SWNTs under special resonance conditions, as discussed below.

In this review we only discuss isolated SWNTs resonant with the *incident* light. In this case, the RBM, the G band and the D and G' bands are all present in the spectra and we can perform a tentative (n, m) assignment based on analysis of the RBM feature and on corroboration from the properties of the G-band, D-band and G'-band spectra [4]. Since the E_{ii} values depend sensitively on both nanotube diameter and chirality, the (n, m) SWNTs that should exhibit special G-band spectra can be predicted by resonance Raman theory.

We show in Figure 16 the RBM and the G-band spectra for three different isolated semiconducting SWNTs coming from three different light spots on the sample. These three tubes all

exhibit similar diameters (d_t 1.60 nm), and the (n, m) indices for each nanotube were determined on the basis of their RBM spectra [16] to yield the diameter and chiral angle for each tube. For all three nanotubes in Figure 16, the incident laser is resonant with the E_{44}^S electronic transition. The spectra in Figure 16 show that the relative intensities between the ω_G^- and the ω_G^+ modes are quite different from one spectrum to another [41].
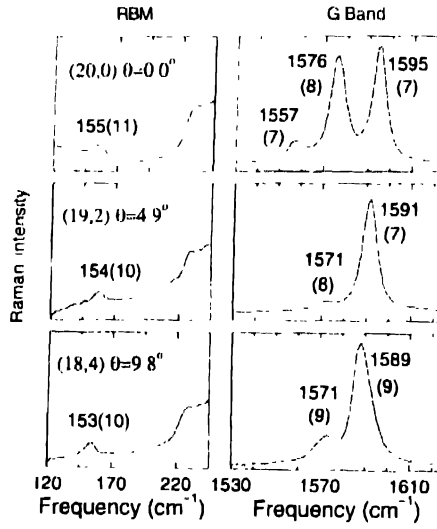

Figure 16. RBM and the G-band Raman spectra for three isolated semiconducting single wall carbon nanotubes with similar diameters ($d_t \sim$ 1.60 nm) that are resonant with the laser ($E_{laser} \sim 2.409$ eV) at three different spots on the sample. The frequencies (widths) of the intense peaks are displayed in cm^{-1}. The shoulder observed to the right side of the RBM spectral feature comes from the Si/SiO$_2$ substrate. The tentative (n, m) indices and respective chiral angles θ for each nanotube are also displayed [41]

To understand the special G-band spectra shown in Figure 16, it is important to consider the (i) the electronic transition

Table 1. Mode frequencies (cm^{-1})/energy (eV) for the scattered photons for the different G-band features observed for the three SWNTs shown in Figure 16 We here use $E_{laser} = 2.409$ eV to calculate $E_{laser} \cdot E_{ph}$. Also displayed in the table are the observed RBM frequency ω_{RBM} (cm^{-1}), the nanotube diameter d_t (nm), nanotube chiral angle θ (degrees), the calculated $\omega_{RBM} = 248/d_t$ (cm^{-1}), and E_{ii}^S (eV) [$i = 3,4$] values for each of the SWNTs in Figure 16 Here we see that $E_{33}^S = 2.22$ for (20,0) is closer to ($E_{laser} - E_{ph}$) for ω_G^- (2.214 eV) and ω_{E_2} (2.216 eV), while E_{44}^S for (19, 2) is closer to ($E_{laser} - E_{ph}$) for ω_G^+ (2.211 eV) (see bold faced numbers)

(n m)	(20,0)	(19,2)	(18,4)
d_t	1.59	1.59	1.61
θ	0.0	4.9	9.8
$248/d_t$	156.2	155.6	153.9
E_{33}^S/E_{44}^S	2.22/2.40	2.21/2.40	2.16/2.39
ω_{RBM}	155	154	153
ω_G^+ ($E_{laser} - E_{ph}$)	1595/2.211	1591/2.211	1589/2.212
ω_G^- ($E_{laser} - E_{ph}$)	1576/2.214	1571/2.214	1571/2.214
ω_{E_2} ($E_{laser} - E_{ph}$)	1557/2.216		

energy E_{ii} is different for different SWNTs, depending on their chirality due to the trigonal warping effect [7]; (ii) the phonon energy E_{ph} is different for different ω_G frequency modes, such as ω_G^+ (1591^{-1} = 198 meV) and ω_G^- (1571 cm^{-1} = 195 meV), and thus the energy $E_{laser} - E_{ph}$ for the scattered photon will also be different for different G-band modes. Therefore, for different SWNTs excited with the same E_{laser} and having almost the same d_t, different phonons may be enhanced differently by a resonance process occurring with the scattered photons. The inset to Figure 17(a) and Table 1 illustrate this picture, as we discuss below [41].
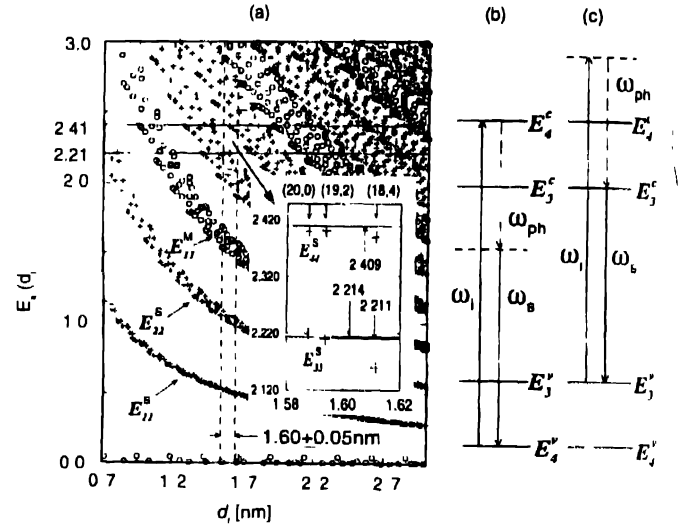
Figure 17. (a) Plot of the electronic transitions E_{ii} for single wall carbon nanotubes vs. nanotube diameters for d_t between $0.7 < d_t < 3$ nm as a function of diameter, obtained from tight binding calculations [6] with $\gamma_0 = 2.90$ eV Crosses give the E_{ii}^S values for semiconducting SWNTs and circles give E_{ii}^M values for metallic SWNTs The inset shows a zoom of the region where the crosses correspond to the E_{33}^S and E_{44}^S electronic transitions for the three SWNTs shown in Figure 16 The vertical lines indicate the incident photon energy $E_{laser} = 2.409$ eV, and the scattered photon energies for $\omega_G^+(E_{laser} - E_{ph} = 2.211$ eV) and $\omega_G^-(E_{laser} - E_{ph} = 2.214$ eV) scattering processes (b) and (c) show schematic figures for the two possible scattering processes for SWNTs with $d_t = 1.60 \pm 0.05$ nm [vertical dashed lines in (a)], where resonance (indicated by the bold arrow) can occur with either (b) the incident photon, or (c) the scattered photon ($E_{laser} - E_{ph} \sim 2.41 - 0.20 = 2.21$ eV) [41].

Figure 17(a) shows the electronic transitions E_{ii} for SWNTs as a function of diameter. The $E_{laser} = 2.41$ eV laser excitation energy is denoted by a horizontal line, as well as the energy level for the Stokes scattered light $E_{laser} - E_{ph} \sim 2.41 - 0.20 = 2.21$ eV. From their RBM features, we assign the tubes shown in Figure 16, from the top to the bottom as (20, 0), (19, 2) and (18,4), and the analysis summarized in Table 1. Although the three SWNTs have similar diameters, they exhibit different chiral angles (see Figure 16), and therefore, due to the trigonal warping effect, they exhibit different E_{ii} values [see Table 1 and the inset to Figure 17(a)]. The frequencies for the various G-band peaks and the expected scattered photon energies are also displayed in Table 1. In the case of the (20,0) and (19,2) SWNTs, the E_{33}^S

alues are within ~ 10 meV of the energies of the scattered photons $(E_{laser} - E_{ph} \sim 2.21$ eV), while for the (18,4) SWNT, the ω_G^- value is far from the scattered photon energies (~ 50 meV). Although the tight binding calculation [6] is not accurate to meV precision, we can say that in the case of the (20,0) SWNT, ω_G^- is closer to the scattered photon energy involving ω_G^- $(E_{laser} - E_{ph} = 2.409 - 0.195 = 2.214$ eV), while in the case of the (19, 2) SWNT, E_{31}^S is closer to the scattered photon energy involving ω_G^+ $(E_{laser} - E_{ph} = 2.409 - 0.198 = 2.211$ eV) [see inset to figure 17(a)]. Note that the lowest frequency mode at 1557 m^{-1} (E_2 symmetry), [35, 42] for the (20, 0) SWNT is also nhanced by the scattered photon resonance that is close to the E_2 and the E_2 symmetry G-bandpeak can be clearly observed see G-band spectrum for the (20,0) SWNT in Figure 16]. The observations show a higher relative enhancement for ω_G^- for the (20,0) SWNT, a higher relative enhancement of the ω_G^+ nature for the (19, 2) SWNT, and the usual lineshape for the (18, 2) SWNT, consistent with predictions for the scattered photon resonance based on the tentative (n, m) assignments [41]. Since the energy difference between modes in the G-band is only a few meV (24 cm^{-1} is equivalent to 3 meV), the observation of this resonance effect indicates that the resonance window is sharp (less than 10 meV), in agreement with the discussion in 14 [17, 19].

In summary, the relative intensities of the G-band features of single wall carbon nanotubes are found to vary from one tube to another, with $I_{\omega_G}/I_{\omega_G^+}$ lying in the range 0.1–0.3 for most of the observed SWNTs (about 90%). However, when the resonance occurs with the scattered photons, the energy difference between the electronic transition E_{ii} and the scattered photon energy $E_{laser} - E_{ph}$ will be different for different frequency phonons (ω_G^- and ω_G^+) associated with different (n, m) SWNTs. If the van Hove singularity of a specific (n, m) SWNT happens to be very close to $E_{laser} - E_{ph}$ for one of the G-band modes, it will be this particular phonon mode that will be strongly enhanced, giving rise to special and unusual G-band profiles

17 Dispersive modes used to probe electronic structure :

In contrast to the *non-dispersive* modes discussed in the previous sections, the *dispersive* modes are special because the resonant processes couples electrons and phonons through a *double resonance* mechanism. This mechanism allows one to probe not only phonons with $q = 0$ (*i.e.*, at the zone center or Γ point) but also phonons within the Brillouin zone. In this section we first describe this mechanism for graphite. After that we discuss how the large dispersion of these modes provides a sensitive probe of quantum effects in the electronic structure, thus establishing resonance Raman spectroscopy in carbon nanotubes as an accurate tool for accessing and probing the electronic structure on a meV scale.

4.7.1 Double Resonance in graphite

Two-dimensional (2D) graphite is a zero band gap semiconductor with a special electronic structure associated with its linear *k*-dependent energy bands for the valence and conduction bands, which cross at the zone edge (*K*-point). Optical processes in the visible range occur around the zone edge and the linear *k* electronic dispersion relations give rise to a very special resonance Raman effect. This effect, called the *double resonance* effect in sp^2 carbon materials, is responsible for activating several phonon modes within the Brillouin zone. The dispersive modes (*D* and *G'* modes) are the modes that have been most intensively studied in sp^2 carbons since the 70's [44]. The disorder-induced *D* mode (one phonon process) requires a defect for one of the intermediate states, while the *G'* (a two phonon process) does not. The resonance process for the *D* band is depicted in Figure 18 (a), and the *G'*-band process, involving two phonons at q and $-q$, is indicated in Figure 18(b). The electrons have initial wave vectors k (measured from the *K* point) in the graphite Brillouin zone, and also a scattered electronic state with wave vector $K + q$ (q is the phonon wavevector), which satisfies the energy-momentum conservation relation

$$E(k+q) = E(k) \pm \hbar\omega_{ph} . \tag{11}$$
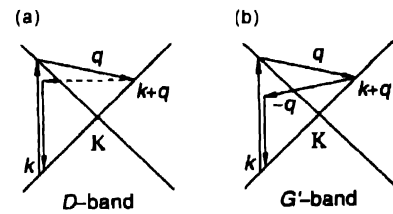
Figure 18. Double resonance Stokes process at the *K* point in the 2D graphite Brillouin zone. (a) The scattering process for activating the Stokes *D* band and where the resonance is with the incident photon.The dashed line indicates the elastic scattering by a defect (b) The scattering process for the Stokes *G'* band. Other possible scattering events, not shown in the figure, involve elastic scattering first and phonon scattering second for the *D*-band, resonance with scattered photons, and anti-Stokes processes [43]

Here ± corresponds to the Stokes and anti-Stokes processes. Energy and momentum conservation requirements select two possible equi-energies $E(k + q)$ where the electrons have $k + q$ wave vectors. One of these equi-energies $E(k+q)$ exists around the same *K* point as the initial state *k* and the second is located around the inequivalent *K'* point in the first Brillouin zone for graphite. After the annihilation of the incident photon, Figure 18(a) ahows an electron in an actual state *k* is scattered to a resonant state $k + q$ and then elastically scattered by an impurity or defect back to a virtual state with the wave vector *k*. After this, the electron-hole pair recombination occurs and the scattered photon is created. The scattering by the phonon and impurity/defect can occur in either order but the intermediate state at ($k + q$) and one of the states at *K* (either the incident or scattered photon at *k*) is also resonant. For the *G'* band, which

involves two phonons with q and $-q$ wave vectors, electrons in the $k + q$ states are now inelastically scattered to a final state with wavevector k.

Of particular importance, the energy and momentum conservation requirements lead to a relation between the k for electrons and the q for phonons By searching for a double resonance that satisfies the condition in Eq (11) within the Brillouin zone of graphite, and by neglecting the trigonal warping effect for simplicity, it is found that q values that strongly contribute to the double-resonance condition are preferentially located near $q \sim 2k$ This relation is special and causes different incident photon energies (E_{laser}) to excite different k states, which in turn change the q phonon wavevector magnitude, thus allowing one to use phonons to probe the electronic dispersion relations through the strong electron-phonon coupling under resonance Raman conditions This simple relation between the electronic wave vectors k and phonon wave vectors q has some restrictions in the case of carbon nanotubes, because of the cutting lines that restrict the number of available states, and this is discussed in the next section

4 7 2 Effect of cutting lines on 1D Raman scattering for dispersive modes

The big advantage of working with dispersive modes is the possibility to probe the phonon dispersion relations of nanometric samples, where inelastic neutron scattering is not suitable for measurements on such kinds of samples. The power of the model that has been proposed for describing the double resonance effect for dispersive bands [10, 45] is that it has been successfully used for achieving a very detailed understanding of the scattering mechanism of the D-band and the G'-band in 2D graphite samples.[46] But this model, as initially proposed, still has limitations, because the resonance Raman measurements lead to an average over the 2D Brillouin zone states, since the resonance occurs for all wavevectors that are on an equi-energy contour that matches the laser energy Thus, for a 2D system, the double resonance technique described above does not reveal details of the phonon structure as a function of wavevector *direction*, being sensitive only to the wavevector *magnitude*. In this scenario, not all the information provided by the experimental results is used, so that improvements in the models cannot profit from all the information that the measurements actually provide. One way to overcome this barrier, is to probe the low-dimensional system directly, whereby the confined states allow one to probe limited regions of phonon reciprocal space.

The pioneering use of this idea was made possible by carrying out measurements on isolated single wall carbon nanotubes. These 1D materials open up a unique opportunity because they are resonantly probed in the experiments through a process involving the confined electronic states that are, in fact, represented by individual points in the Brillouin zone of 2D graphite. More than that, these individual points are unique for each different nanotube and the points exhibit an angular dependence on chiral angle θ due to trigonal warping effect as

discussed in §4.3. By this approach it is now possible to establish a resonance Raman process that is sensitive to both magnitude (laser energy magnitude) and direction (different chiralities) of the phonon wavevector. The measurements of several individual points in the 2D Brillouin zone, *i.e.*, measured with many different nanotubes in the laboratory, provide access to very detailed information about the phonon structure within the Brillouin zone, thereby allowing us to learn how to improve the model calculations, and to learn not only about the new scattering phenomena, but also about the materials themselves.

In the case of graphite, the electronic valence and conduction bands cross at the hexagonal corner (K point) of the first Brillouin zone of a single graphitic layer [see Figure 8(b)], and thus the electronic equi-energy contours represent circles around the K point in reciprocal space (see Figure 19). However, the shapes of the contours deviate from circles further away from the K point, *i.e.*, with increasing laser excitation energy, and these contours become triangularly distorted. This phenomenon is well known in carbon nanotube science as a trigonal warping effect [7] Due to this trigonal warping effect, the van Hove singularities (VHSs) in the DOS of carbon nanotubes of the same diameter but different chiralities diverge from each other as the electronic wave vector moves away from the K point [see Figure (b)], thus making it possible to identify the nanotube structural indices (n, m) by resonance Raman spectroscopy (see §4 3)[16].
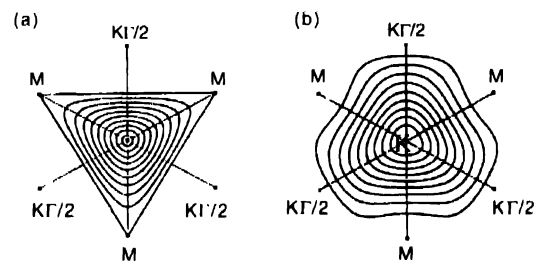

Figure 19. (a) The electronic equi-energy contours and (b) the phonon equi-frequency contours for 2D graphite in the vicinity of the hexagonal corner K of the Brillouin zone [43]

Like the electronic equi-energy contours, the phonon equi-frequency contours also exhibit distortions from a simple circular shape. As was shown recently, the double resonance nature of the dispersive Raman bands, which is selective of the wavevector magnitude, can be successfully combined with the wavevector direction selectivity, which arises from the low dimensionality of the carbon nanotubes, thus allowing us to probe directly the phonon equi-frequency contours of graphite and to measure the phonon trigonal warping effect [43]. The electronic equi-energy contours and the phonon equi-frequency contours are shown in Figures 19(a) and (b), correspondingly The anisotropy observed in the phonon equi-frequency contours appears explicitly in the Raman spectra of carbon nanotubes in the form of a two-peak structure of the dispersive Raman features, as described below.

4.7.3 Two-Peak Raman Structures for Semiconducting and Metallic SWNTs

An anomalous two-peak structure of the G'-band Raman feature has been observed for both semiconducting [47] and metallic- [48] SWNTs. The phonon anisotropy, or the phonon trigonal warping effect, is responsible for the appearance of two peaks in the double resonance Raman features of metallic SWNTs, while a different mechanism gives rise to a similar effect for semiconducting SWNTs.[47] Semiconducting and metallic SWNTs may both have two VHSs within the resonant window of the incident and scattered light, as shown in Figures 20(a) and (b) for semiconducting (17,6) and metallic (27,0) nanotubes, correspondingly. Each of the two resonant VHSs give rise to a different peak in the double resonance Raman features, as shown in Figures 20 (c) and (d). In the case of semiconducting SWNTs,
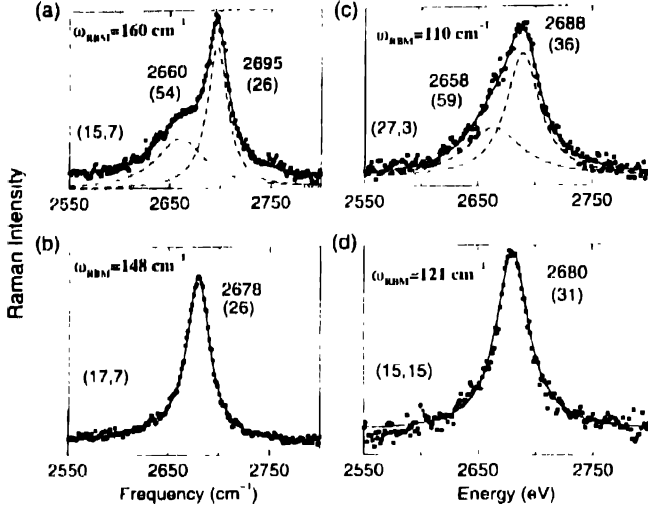

the K point is located at a distance between two adjacent cutting lines, which is in the ratio of 1:2 (see Figure 20(a)), and thus the wavevectors for the two resonant VHSs (k_3 and k_4 in Figure 20 (a)) have a difference in their magnitudes which is equal to 1/3 of the distance between the two adjacent cutting lines[6]. This difference in the magnitudes of the electronic wavevector (k) results in a two times larger difference in the resonance phonon wavevector (q) magnitudes, due to the double resonance condition $q = -2k$ on the wavevectors [49]. The difference in the phonon wavevector magnitudes results in a difference in the phonon frequencies, and therefore in the Raman shifts, as shown in Figure 20(c). This difference arises from the dispersion of the phonon branches (the G-band phonon branch).

The case of the two-peak feature for metallic SWNTs differs in the sense that one of the cutting lines crosses the K point, as shown in Figure 20 (b), so that the two wavevectors corresponding to the two resonant VHSs that are located at the two different sides at the *same* distance from the K point. These two wavevectors therefore have the *same magnitude* but opposite *directions*. [a]

Thus, the phonon wavevectors also have the same magnitudes and opposite directions, and for metallic SWNTs the difference between the two resonant VHSs arises, not from the difference in the magnitudes of the resonant electronic wavevectors, but rather from the difference in the directions of the resonant electronic wavevectors, *i.e.* from the electronic trigonal warping effect, which predicts different electronic energies for the phonon wavevectors of the same magnitude and opposite directions. Similarly, the double-peak structure of the dispersive Raman features in metallic nanotubes (see Figure 20 (d)) arises not from the phonon dispersion, but rather from the phonon trigonal warping effect. Thus, theory tells us that similar experimental observations of a splitting of the double resonance Raman features have different origins in the cases of semiconducting and metallic carbon nanotubes. For semiconducting nanotubes, the double-peak structure arises from the phonon dispersion, while for metallic nanotubes, the double-peak structure arises from the anisotropy in the phonon dispersion relations, or the phonon trigonal warping effect.

After presenting the theory on the effect of cutting lines for the dispersive mode profiles, we now present some experimental results for isolated semiconducting and metallic nanotubes. We focus our analysis on the G' band (rather than the D-band), because the G' band exhibits a larger dispersion and the effects associated with this dispersion are more easily accessible, because the features can be experimentally resolved. By carrying out experiments on several isolated tubes, some of the G' band features for both metallic and semiconducting tubes are found to exhibit a two-peak profile (see Figure 21), whereas other tubes have just a single peak. In the case of semiconducting tubes, the two-peak structure is associated with the different quantized wavevectors k_i and k_{i-1} involving the incident and scattered

Figure 20. Cutting lines for (a) semiconducting (17, 6) and (b)metallic (27, 0) SWNTs. Two equi-energy contours in (a) and (b) are shown for resonance with the incident $E_{laser} = 2.41$ eV and with the 2.08.eV photons scattered by G'-band phonons. The superscripts indices *l* and *u* in (b) stand for lower and upper energy components of the van Hove singularity. l^u. The meaning of '15K', 'θ' and '3KM' is that the indicated points on the figure are 0.15 and 0.30 of the distance from K to θ and from K to M respectively. The corresponding two-peak structures predicted for the double resonance Raman features in the spectra for the G'-bands are shown in (c) and (d), for the semiconducting (17,6)and the metallic (27,0) nanotubes and values for the energies of the pertinent van Hove singularities are given [43]

[a] Strictly speaking, this is not exactly the case. Due to the electronic trigonal warping effect, both resonant wavevector magnitudes and resonant wavevector directions differ from the simple model presented above. [b] $|k_i| = |K_i|/3$ for semiconducting nanotubes and $|k_i'| = |k_i'|$ for metallic nanotubes, and thus both the effects of the phonon dispersion [the phonon anisotropy give rise to the two-peak structure of the dispersive Raman features. In the vicinity of the K point, *i.e.*, for smaller excitation energies, the trigonal warping effect is weak, and therefore the two peak structure or the G'-band splitting for metallic nanotubes is covered mostly by the phonon anisotropy and for the semiconducting nanotubes mostly by the phonon dispersion. Further away from the K point, *i.e.*, at higher laser excitation energies, the two-peak structure splitting for both metallic and semiconducting nanotubes is no longer covered by pure phonon anisotropy or phonon dispersion effects, but rather by both anisotropy and dispersion.

photons of the double resonance process, respectively, as shown in the experimental spectra for the semiconducting (15,7) tube in Figure 21 (a). When only one quantized wavevector k_j is involved, as in the case of the (17,7) tube, where only the k_1 wavevector is involved,only one peak is observed, as depicted in Figure 21 (b) [47]


Figure 21. G'-band peak profiles for semiconducting tubes in (a) and (b) [47], and for metallic tubes in(c) and (d) [48] Two-peak profiles are observed in (a) and (c) and one peak profiles in (b) and (d) The frequencies (linewidths) are listed in units of cm⁻¹

In the case of metallic tubes, the two-peak structure arises from the same quantized subband i, and involves two van Hove singularities that are split by the trigonal warping effect, as discussed above. This effect is indeed chirality dependent and goes from a single peak for $\theta = 30°$ (armchair tube) to a maximum splitting for $\theta = 0°$ (zigzag tube) [see Figure 3(a)]. It is striking that these peaks in the electronic structure connect with phonons via the double resonance mechanism, thus giving rise to different profiles for the experimental G'-band spectra [48], and this effect for metallic tubes is illustrated, for example, with the (27,3) and (15, 15) tubes [see Figure 21(c) and (d)], for which two-peak and one-peak profiles are observed, respectively, thus supporting the theoretical framework discussed above for cutting line effects on the profile of the dispersive G'-band feature. On the basis of these phenomena, the profile of the G'-band mode is then used to probe singular points in the 2D Brillouin zone of graphite, and this phenomena is discussed in §4.8

4.8 Trigonal warping of the phonon constant energy surfaces:

Resonance Raman scattering in a graphene layer involves all the electronic states with wavevectors along the equi-energy contour corresponding to a given laser excitation energy. The three equi-energy contours corresponding to the three E_{laser} values 1.58eV, 2.41eV, and 2.54 eV commonly used in Raman spectroscopy studies are plotted in Figure 22, where k-space in the vicinity of the K point in the 2D BZ of graphite is shown. Compared to the case of graphite, the number of electronic states

in SWNTs is limited by quantum confinement to a subset of *allowed states*, which can be picked out by the zone-folding method [6]. For each SWNT, the allowed states are located along cutting lines. The distance between adjacent cutting lines $|K_1| = 2/d_t$ is inversely proportional to the SWNT diameter d_t while the orientation of the cutting lines is given by the SWNT chiral angle θ between them and the line connecting the Γ points in the 2D BZ [6]. Four cutting lines are shown in Figure 22 by gray lines on either side of the K point,two for zigzag (θ = 0) and two for armchair ($\theta = \pi/6$) SWNTs. The van Hove singularities (VHSs) in the density of states (DOS) of SWNTs appear at points k_j in the 2D BZ where, the cutting lines are tangential to the equi-energy contours. When the SWNT chirality changes from $\theta = 0$ to $\pi/6$, the two k_j vectors at the VHSs on either side of the K point move along the equi-energy contour, taking all possible directions away from the K point, such as $K\Gamma$ and KM for zigzag SWNTs, and two equivalent directions between $K\Gamma$ and KM for armchair SWNTs (see Figure 22). Accordingly, the resonant phonon wavevectors q_i also take all possible directions away from the K point, because of the coupling between the resonant electronic and phonon wavevectors $q_i = -2k_i$ in the double resonance process [49]
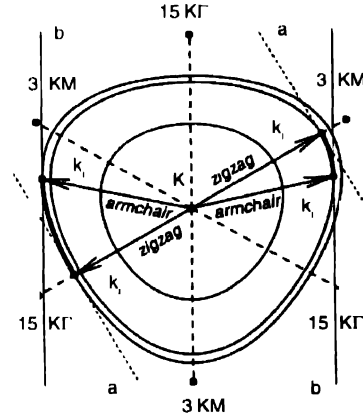

Figure 22. The electronic wavevectors k_j of the VHSs in SWNTs of zigzag (a) and armchair (b) structural symmetries. The cutting lines for the armchair tubes are vertical solid gray lines labeled 'b' and for zigzag tubes the cutting lines (dotted gray lines labeled 'a') make an angle of 30° with the vertical Three equi-energy contours are shown for the three laser energies 1.58 eV, 2.41 eV, and 2.54 eV [43].

Thus, by combining the double resonance process with the low dimensionality of carbon nanotubes, a procedure is obtained that is selective not only of the wavevector magnitude in the 2D reciprocal space of graphite, as is known for the case of graphite and SWNT bundles [10], but also is selective of the wavevector *direction* in the 2D reciprocal space [43].While the wavevector *magnitude* is selected by the laser excitation energy as for the case of graphite and SWNT bundles [10], the wavevector *direction* is selected by the SWNT chiral symmetry, changing from the KM and $K\Gamma$ directions for zigzag SWNTs to an intermediate direction between KM and $K\Gamma$ for armchair SWNTs [43].

Anisotropy in the phonon dispersion relations, or the phonon trigonal warping effect, has been probed for the D/G' phonon modes by resonance Raman spectroscopy on isolated SWNTs, following the procedure briefly described above [43] Among many isolated SWNTs from which Raman spectra were recorded, 11 SWNTs have been selected which show strong G'-band Raman features, and best satisfy the preresonant condition of the type shown in Figure (b) to ensure the probing of an individual point in the BZ and to allow an (n, m) assignment to be made for a further determination of the resonant electronic and phonon wavevectors k_r and $q_r = -2k_r$. The G'-band features measured from these 11 SWNTs have been fitted with Lorentzian peaks, and the frequencies have been upshifted by 35.4 cm nm/ d_t to account for the softening of the force constants due to the curvature of the SWNT surface [50]. The phonon frequencies are then divided by 2 since there are two phonons involved in the G'-band process. The resulting phonon frequenciesas a function of the phonon wavevector q_r in the 2D BZ along with previously reported measurements on HOPG, graphite whiskers, and SWNT bundles for the other phonon modes have been used to fit the calculated phonon dispersion relations using a nonlinear least squares minimization of the functional made of

the differences between the observed and calculated phonon frequencies [51]

The resulting phonon dispersion shows significant anisotropy around the K point in the 2D BZ, as shown in Figure 23. Solid lines in Figure 23 show the phonon dispersion relations as a function of phonon wavevector (a) magnitude and (b) direction, while the dashed lines show the corresponding electronic dispersion dependences on electronic wavevector (a) magnitude and (b) direction. The lower and left scales in Figure 23 (a) and (b) correspond to the phonon wavevector and frequency, and the upper and right scales to the electronic wavevector and energy. Two different curves in Figure 23 (a) correspond to the opposite directions KM and $K\Gamma$ for the wavevector in the 2D BZ. The wavevector magnitude $q_0 = 2k_0 = 0.24\ K\Gamma$ in Figure 23 (b) corresponds to the laser excitation energy of 2.41 eV, shown by the central vertical line in Figure 23 (a). Symbols in Figure 23 (b) correspond to the experimentally measured phonon frequencies for 11 SWNTs, and different symbols correspond to different interband transitions, as shown in Figure 23(b). From Figures 23 (a) and (b),one can clearly see the anisotropies of the electronic and
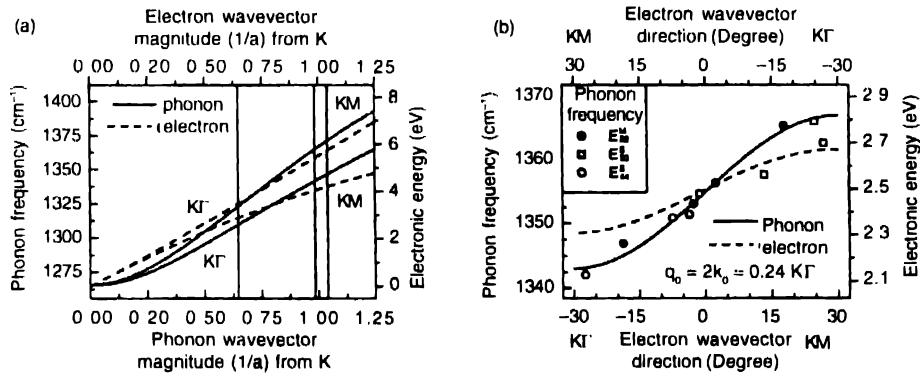
Figure 23. The solid/dashed lines show the fitted phonon frequency for the D-band phonon mode/ electronic energy (left/right scales)as a function of (a) the magnitude of the phonon/electron wavevector measured from the K point in the 2D BZ (lower/upper scales) and (b) the direction of the phonon/ electron wavevector measured from the K point in the 2D BZ (lower/upper scales). Vertical lines in (a) correspond to the phonon wavevectors (lower scale) excited in the double resonance processes with the laser energies of 1.58 eV, 2.41 eV, and 2.54 eV that are commonly used in Raman spectroscopy studies of carbon nanotubes The symbols in (b) are the phonon frequencies from experimental Raman scattering data (lower and left scales) [43]

phonon equi-energy and equi-frequency contours around the K point. For a quantitative comparison between the phonon and electronic anisotropies, one can see from Figure 23 (b) that the difference between the phonon frequencies for the opposite directions of the phonon wavevector KM and $K\Gamma$ is equal to24 cm^{-1}. The phonon frequency changes by 89 cm^{-1} from $q = 0$ (the K point) to $q = q_0 = 0.24\ K\Gamma$, and thus the magnitude of the phonon trigonal warping effect is given by 24 cm^{-1}/89 cm^{-1} = 27%. Similarly, the magnitude of the electronic trigonal warping effect from Figure 23(b) is given by 0.36 eV/2.49 eV=14%. The magnitude of the electronic trigonal warping effect in this figure is some what smaller than the magnitude of the phonon trigonal

warping effect, in part[5] because of the factor of 2 in the double resonance condition $q_i = -2k_i$.

4.9 Double resonance-induced combination and overtone modes:

In this section we show how resonance Raman spectroscopy in carbon nanotubes allow one to precisely assign the combination and overtone modes due to the highly selective scattering imposed by the electronic structure and double resonance. This is a unique situation compared to bulk 3D systems, where such second-order modes cannot always be clearly assigned.

Second-order combination and overtone modes in highly ordered pyrolytic graphite (HOPG), in single wall carbon nanotube (SWNT) bundles, and in isolated SWNTs have been observed. Dispersive and non-dispersive Raman bands in the range 1650–2100 cm^{-1} have been observed, and the frequency vs. laser energy E_{laser} behavior of these features are in agreement with predictions from double resonance Raman theory. In the case of SWNTs, these second-order bands depend on the one-dimensional structure of SWNTs, and, at the single nanotube level, the spectra vary from tube to tube, depending on tube diameter and chirality, and on the energy of the van Hove singularity relative to E_{laser} [11].

Raman spectroscopy has already proven to be a powerful technique to study carbon materials [52], including single wall carbon nanotubes (SWNTs) through the diameter selective resonance Raman effect [18, 28]. It has been known for some time [52] that graphite-related materials exhibit a rich Raman spectra, with several first- and second-order features, disorder-induced bands, some of them being dependent on laser excitation energy E_{laser}. However, many of these features remained unexplained for a long time. It is only recently that the appearance of these features and their dependence on E_{laser} were explained as due to a double resonance process that enhances the scattering of light by certain modes in the interior of the Brillouin zone ($q \neq 0$) of graphite-related materials [10, 11, 51, 53]. Weak Raman features observed in the frequency range 1650–2100 cm^{-1} in graphite-related materials (i.e., HOPG, SWNT bundles and isolated SWNTs) have been identified with the overtones and combination modes of the several phonon branches in graphite, as predicted by double resonance theory [10, 53].

In particular, a multi-featured band at about 1750 cm^{-1} has been observed in HOPG [54], in irradiated graphite [55], and in SWNT bundles [56], and has been assigned to an overtone of the infrared-active out-of-plane (oTO) mode at 867 cm^{-1} in graphite. Another very highly dispersive mode at higher frequencies (around 1950 cm^{-1}) that has previously been reported for SWNT bundles [57], and this feature has been tentatively identified as a combination of the in-plane transverse optic (iTO) and longitudinal acoustic (LA) modes, namely (iTO+LA). Thus, the results for both the features around 1750 cm^{-1} and the feature around 1950 cm^{-1} have been identified as combination modes

[10, 53]. In the case of isolated SWNTs, the multi-featured band at 1750 cm^{-1} shows a richer behavior than in HOPG (and is more complicated than the D-band and the G'-band in isolated SWNTs [47, 58]), varying from tube to tube, thus suggesting a strong dependence on the one-dimensional structure of SWNTs [11]

5. Conclusion

In summary, this review article has focused on novel resonance Raman effects related to one-dimensional structures, which have been illustrated through the model 1D carbon nanotube system. Due to the strong electron-phonon coupling and the quantum confinement of electrons and phonons in 1D systems, interesting effects are observed, such as asymmetries in the Stokes/anti-Stokes spectra, line-shape dependent effects associated with how well the system satisfies the resonance condition, and many other unusual results. Analysis of these effects give detailed information about the confined phonon and electron states, showing that resonance micro-Raman spectroscopy of phonon modes can determine electronic and even structural properties in 1D-systems. Carbon nanotubes were used as a model 1D system because they are the best prototype for 1D materials presently available, but the theoretical and experimental findings can be considered more broadly in future work for studying resonance Raman spectroscopy in 1D systems in general. Finally, it is also shown that the resonance Raman effect provides a useful technique for obtaining phonon dispersion relations for nanoscale samples, and that measurements on low-dimensional systems can be used to obtain important information about related higher dimensional systems that would otherwise be difficult to obtain.

References

[1] C V Raman *A new radiation*, *Indian J Phys* **2** 387-398 (1928), reprinted in *Curr. Sci. India* **74** (4) 382-386 FEB 25 1998

[2] C V Raman *Proc. Indian Acad. Sci.* **A34** 61 (1951)

[3] C V Raman *Proc. Indian Acad. Sci.* **A44** 99 (1956)

[4] M S Dresselhaus, G Dresselhaus, A Jorio, A G Souza Filho and R Saito *Raman spectroscopy on isolated single wall carbon nanotubes*, *Carbon* **40** 2043 (2002)

[5] G Herzberg *Molecular Spectra and Molecular Structure* (Princeton, NJ : Van Nostrand) (1945)

[6] R Saito, G Dresselhaus and M S Dresselhaus *Physical Properties of Carbon Nanotubes*, (London : Imperial College Press) (1998)

[7] R Saito, G Dresselhaus and M S Dresselhaus *Trigonal warping effect of carbon nanotubes*, *Phys Rev* **B61** 2981 (2000)

[8] R M Martin and L M Falicov *Light Scattering in Solids*, Edited by M Cardona, Vol. **8** of *Springer Series in Topics in Applied Physics*, Vol.8 (Berlin : Springer-Verlag) (1981)

[9] C Thomsen and S Reich *Double resonant Raman scattering in graphite* *Phys Rev Lett* **85** 5214 (2000)

[10] R Saito, A Jorio, A G Souza Filho, G Dresselhaus, M S Dresselhaus and M A Pimenta *Probing phonon dispersion relations of graphite by double resonance Raman scattering*, *Phys Rev Lett* **88** 027401 (2002)

[11] V W Brar, G G Samsonidze, G Dresselhaus, M S Dresselhaus, R Saito, A K Swan, M S Unlu, B B Goldberg, A G Souza Filho and A Jorio *Second-order harmonic and combination modes in graphite, single-wall carbon nanotube bundles, and isolated single-wall carbon nanotubes* *Phys Rev* **B66** 155418 (2002)

[12] R Saito, M Fujita, G Dresselhaus and M S Dresselhaus *Electronic structures of carbon fibers based on C₆₀, *Phys Rev* **B46** 1804 (1992)

[13] R Saito, M Fujita, G Dresselhaus and M S Dresselhaus *Electronic structure of chiral graphene tubules*, *Appl Phys. Lett* **60** 2204 (1992)

[14] M F Lin *Optical spectra of single-wall carbon nanotube bundles*, *Phys Rev* **B62** 13153 (2000)

[15] A Grüneis, R Saito, G G Samsonidze, T Kimura, M A Pimenta, A Jorio, A G S Filho, G Dresselhaus and M S Dresselhaus, *Inhomogeneous optical absorption around the K point in graphite and carbon nanotubes*, *Phys Rev* B Submitted 07/17/02; MS BU8254

[16] A Jorio, R Saito, J H Hafner, C M Lieber, M Hunter, T McClure, G Dresselhaus, M S Dresselhaus, *Structural (n, m) determination of isolated single-wall carbon nanotubes by resonant Raman scattering*, *Phys Rev. Lett.* **86** 1118 (2001)

[17] A Jorio, A G Souza Filho, G Dresselhaus, M S Dresselhaus, R Saito, J H Hafner, C M Lieber, F M Matinaga, M S S Dantas and M A Pimenta *Joint density of electronic states for one isolated single-wall carbon nanotube studied by resonant Raman scattering*, *Phys. Rev.* **B63** 245416-1 (2001)

[18] A M Rao, E Richter, S Bandow, B Chase, P C Eklund, K W Williams, S Fang, K R Subbaswamy, M Menon, A Thess, R E Smalley, G Dresselhaus and M S Dresselhaus *Diameter-selective Raman scattering from vibrational modes in carbon nanotubes*, *Science* **275** 187 (1997)

[19] M Milnera, J Kürti, M Hulman and H Kuzmany *Periodic resonance excitation and intertube interaction from quasi-continuous distributed helicities in single-wall carbon nanotubes*, *Phys Rev Lett* **84** 1324 (2000)

[20] R Saito and H Kataura, *Optical properties*, M S Dresselhaus, G Dresselhaus and P Avouris (Eds), *Carbon Nanotubes: Synthesis, Structure, Properties and Applications*, Vol. **80** (Berlin : Springer-Verlag) (2001) p 213 (*Springer Series in Topics in Applied Physics*, Vol. **80**)

[21] H Kataura, Y Kumazawa, Y Maniwa, I Umezu, S Suzuki, Y Ohtsuka and Y Achiba, *Optical properties of single-wall carbon nanotubes*, *Synthetic Metals* **103** 2555 (1999)

[22] G Dresselhaus, M A Pimenta, R Saito, J-C Charlier, S D M Brown, P Corio, A Marucci and M S Dresselhaus, *On the π - π overlap energy in carbon nanotubes*, D Tománek, R J Enbody (Eds), *Science and Applications of Nanotubes*, (New York : Kluwer Academic) (2000) p.275, *Proceedings of the International Workshop on the Science and Applications of Nanotubes, Michigan State University, East Lansing, MI, USA, July 24-27*, (1999)

[23] A G Souza Filho, A Jorio, J H Hafner, C M Lieber, R Saito, M A Pimenta, G Dresselhaus and M S Dresselhaus *Electronic transition energy E₍ᵢᵢ₎ for an isolated (n, m) single-wall carbon nanotube obtained by anti-Stokes/Stokes resonant Raman intensity ratio*, *Phys Rev* **B63** 241404R (2001)

[24] Z Yu and L E Brus (n, m) *structural assignments and chirality dependence in single-wall carbon nanotube Raman scattering J Phys Chem.* **B105** 6831 (2001)

[25] J W G Wildoer, L C Venema, A G Rinzler, R E Smalley, C Dekker, *Electronic structure of carbon nanotubes investigated by scanning tunneling spectroscopy*, *Nature* (London) **391** 59 (1998)

[26] T W Odom, J L Huang, P Kim, C M Lieber, *Atomic structure and electronic properties of single-walled carbon nanotubes*, *Nature* (London) **391** 62 (1998)

[27] M A Pimenta, A Marucci, S Empedocles, M Bawendi, E B Hanlon, A M Rao, P C Eklund, R E Smalley, G Dresselhaus and M S Dresselhaus *Raman modes of metallic carbon nanotubes*, *Phys Rev B Rapid* **58** R16016-R16019 (1998)

[28] M S Dresselhaus and P C Eklund *Phonons in carbon nanotubes*, *Adv. in Phys* **49** 705 (2000)

[29] S D M Brown, P Corio, A Marucci, M S Dresselhaus, M A Pimenta and K Kneipp *Anti-Stokes Raman spectra of single-walled carbon nanotubes Phys Rev B Rapid* **61** R5137 (2000)

[30] A Jorio, C Fantini, M S S Dantas, M A Pimenta, A G Souza Filho, G G Samsonidze, V W Brar, G Dresselhaus, M S Dresselhaus, A K Swan, M S Unlü, B B Goldberg and R Saito *Line width of the Raman features of individual single-wall carbon nanotubes Phys Rev* **B 66** 115411 (2002)

[31] A M Rao, P C Eklund, S Bandow, A Thess and R E Smalley *Evidence for charge transfer in doped carbon nanotube bundles from Raman scattering*, *Nature* (London) **388** 257 (1997)

[32] M A Pimenta, A Marucci, S D M Brown, M J Matthews, A M Rao, P C Eklund, R E Smalley, G Dresselhaus and M S Dresselhaus *Resonant Raman effect in single-wall carbon nanotubes J Mater. Res* **13** 2396 (1998)

[33] D Kahn and J P Lu, *Vibrational modes of carbon nanotubes and nanoropes Phys Rev.* **B 60** 6535 (1999)

[34] R Saito, T Takeya, T Kimura, G Dresselhaus and M S Dresselhaus *Raman intensity of single-wall carbon nanotubes Phys. Rev.* **B 57** 4145 (1998)

[35] A Jorio, G Dresselhaus, M S Dresselhaus, M Souza, M S S Dantas, M A Pimenta, A M Rao, R Saito, C Liu and H M Cheng *Polarized Raman study of single-wall semiconducting carbon nanotubes Phys Rev. Lett.* **85** 2617 (2000)

[36] A Kasuya, Y Sasaki, Y Saito, K Tohji, Y Nishina Evidence for size dependent discrete dispersions in single-wall nanotubes, Phys Rev Lett 78 4434 (1997)

[37] R Saito, A Jorio, J H Hafner, C M Lieber, M Hunter, T McClure, G Dresselhaus and M S Dresselhaus Chirality dependent G-band Raman intensity of carbon nanotubes Phys Rev B 64 (2001)

[38] R Saito, A Jorio, G Dresselhaus and M S Dresselhaus Chirality dependence of Raman intensity for carbon nanotubes in N Miura, T Ando (Eds.), Proceedings of the 25th International Conference on The Physics of Semiconductors, Osaka, Vol. Springer Proceedings in Physics 87, (Springer Berlin) p 1629 (2000)

[39] M Damnjanovic, I Milosevic, T Vukovic and R Sredanovic Full symmetry, optical activity, and potentials of single-wall and multiwall nanotubes Phys Rev B60 2728 (1999)

[40] O E Alon Number of Raman- and infrared-active vibrations in single-walled carbon nanotubes Phys Rev B63 201403(R) (2001)

[41] A Jorio, A G Souza Filho G Dresselhaus, M S Dresselhaus, A K Swan, M S Unlu B Goldberg, M A Pimenta, J H Hafner, C M Lieber and R Saito G band resonant Raman study of 62 isolated single wall carbon nanotubes, Phys Rev B65 155412 (2002)

[42] C Fantini M A Pimenta M S S Dantas, D Ugarte, A M Rao, A Jorio, G Dresselhaus and M S Dresselhaus Micro-Raman investigation of aligned single wall carbon nanotubes Phys Rev B63 161405 (2001)

[43] G G Samsonidze, R Saito, A Jorio, A G Souza Filho, A Gruneis, M A Pimenta, G Dresselhaus and M S Dresselhaus Phonon trigonal warping effect in graphite and carbon nanotubes, Phys Rev Lett (2003) in press

[44] F Tuinstra and J L Koenig Raman scattering in disordered graphite, J Phys Chem 53 1126 (1970)

[45] C Thomsen, S Reich, A R Goni, H Jantoljak, P M Rafailov, I Loa, K Syassen, C Journet and P Bernier Intermolecular interaction in carbon nanotube ropes, Phys stat solidi B215 435 (1999)

[46] L G Cancado M A Pimenta, R Saito A Jorio, L O Ladeira, A Gruneis A G Souza Filho G Dresselhaus and M S Dresselhaus, Stokes and anti-Stokes double resonance Raman scattering in two dimensional graphite, Phys Rev B66 035415 (2002)

[47] A G Souza Filho, A Jorio, A K Swan, M S Unlu, B B Goldberg, R Saito, J H Hafner C M Lieber, M A Pimenta, G Dresselhaus and M S Dresselhaus Anomalous two-peak G band Raman effect in one isolated single wall carbon nanotube, Phys Rev B 65 085417 (2002)

[48] A G Souza Filho, A Jorio, G G Samsonidze, G Dresselhaus, M S Dresselhaus, A K Swan, M S Unlu B B Goldberg, R Saito, J H Hafner, C M Lieber and M A Pimenta Probing the electronic trigonal warping effect in individual single wall carbon nanotubes using phonon spectra Chem Phys Lett 354 62 (2002)

[49] R Saito, A Jorio, A G Souza Filho, G Dresselhaus, M S Dresselhaus, A Gruneis, L G Cancado and M A Pimenta First and second order resonance Raman process in graphite and single wall carbon nanotube, Jpn J Appl Phys Part 1 41 4878 (2002)

[50] A G Souza Filho, A Jorio G G Samsonidze, G Dresselhaus M A Pimenta, M S Dresselhaus, A K Swan, M S Unlu, B B Goldberg and R Saito D-band properties of isolated single wall carbon nanotubes, Phys Rev B66 (in press) (2003)

[51] A Gruneis, R Saito, T Kimura, L G Cancado, M A Pimenta, A Jorio, A G Souza Filho, G Dresselhaus and M S Dresselhaus, Determination of two dimensional phonon dispersion relation of graphite by Raman spectroscopy, Phys Rev B65 155405-1 (2002)

[52] M S Dresselhaus, G Dresselhaus, K Sugihara, I L Spain and H A Goldberg Graphite Fibers and Filaments, Vol 5 of Springer Series in Materials Science, (Berlin Springer-Verlag) (1988)

[53] C Thomsen and S Reich Double resonant Raman scattering in graphite, Phys Rev Lett 85 5214 (2000)

[54] Y Kawashima and G Katagiri Observation of the out-of-plane mode in the Raman scattering from the graphite edge plane Phys Rev B59 62 (1999)

[55] M Bonelli, A Miotello, P M Ossi, A Pessi and S Gialanella Laser-irradiation-induced structural changes on graphite, Phys Rev B59 13513 (1999)

[56] L Alvarez, A Righi, S Rols, E Anglaret and J L Sauvajol Excitation energy dependence of the Raman spectrum of single-walled carbon nanotubes, Chem Phys Lett, 320 441 (2000)

[57] S D M Brown, P Corio, A Marucci, M A Pimenta, M S Dresselhaus and G Dresselhaus Second-order resonant Raman spectra of single-walled carbon nanotubes, Phys Rev B61 7734 (2000)

[58] A G Souza Filho, A Jorio, G Dresselhaus, M S Dresselhaus, R Saito, A K Swan, M S Unlu, B B Goldberg, J H Hafner, C M Lieber and M A Pimenta Effect of quantized electronic states on the dispersive Raman features in individual single wall carbon nanotubes, Phys Rev B65 035404-1 (2002)

About the Authors

M S DRESSELHAUS was born on November 11, 1930 in Brooklyn, NY and received her PhD degree in physics from the University of Chicago in 1958. After a two year postdoc at Cornell University, she came to MIT Lincoln Laboratory as a staff member and has been on the MIT faculty since 1967. She is an Institute Professor of Electrical Engineering and Physics at MIT with broad interest in carbon science since 1961, and has been involved in carbon nanotube research since 1991 and carbon fiber research since 1980.

G DRESSELHAUS was born on November 7, 1929 in Ancon, Panama Canal Zone and received his PhD degree in physics from the University of California in 1955. He served one year as an instructor at the University of Chicago, and four years as an Assistant Professor at Cornell before joining MIT Lincoln Laboratory in 1960 as a staff member. In 1977 he was transferred to the MIT Francis Bitter Magnet Laboratory where he is currently a Senior Scientist. His area of interest is the electronic structure of solids. He also has been broadly involved in carbon research since 1955 and carbon nanotube research since 1991, and has co-authored with M. S Dresselhaus several books on carbon materials.

A M RAO was born on February 15, 1961 in Bombay, India and received his PhD degre in condensed matter physics from the University of Kentucky (UKY) in 1989 After a two-year postdoctoral appointment at MIT, he returned to UKY as a Research Assistant Professor until

2000 He is currently at Clemson University as an Associate Professor and has been working on carbon science since 1985.

A IORIO was born on June 11, 1972, in Brazil and received his PhD degree in physics from the Federal University of Minas Gerais, Brazil, in 1999. While completing his PhD, he spent one year (1998) working with Dr Roland Currat, at the Laue-Langevin Institute, France. He worked for two years (2000 and 2001) with Professor M S Dresselhaus at MIT, as a postdoctoral fellow. He is currently an Associate Professor of Physics at the Federal University of Minas Gerais, Brazil.

A G SOUZA FILHO was born on June 12, 1975, in Brazil and received his PhD degree in physics from the Federal University of Ceara, Brazil, in 2001. In 2001, he joined the Dresselhaus group at MIT as a PhD visiting student, where he worked for 10 months on single carbon nanotube Raman spectroscopy. He is currently an associate researcher at the Federal University of Ceara working on aspects of Raman Scattering in solids.

GE G SAMSONIDZE was born on August 8, 1976, in the Soviet Union and received his Master's degree in physics from the Saint Petersburg State Technical University, Russia, in 1999. He joined the Dresselhaus group in 2001 as a PhD student in the Department of Electrical Engineering and Computer Science at MIT. He is currently working on single carbon nanotube Raman spectroscopy.

R SAITO was born on March 13, 1958, in Tokyo. He graduated (B S.) from Tokyo University and earned his Ph.D. there in 1985. After being a research associate at Tokyo University, Saito was an Associate Professor at the University of Electro-Communication in Tokyo from 1990-2002 and recently was named Full Professor at Tohoku University in Sendai. He has worked extensively on the theory of carbon nanotubes since 1991 and has written a book on the subject in collaboration with G and M S Dresselhaus, "Physical Properties of Carbon Nanotubes," published by Imperial College Press, in 1998. He was the recipient of the Japan IBM prize in 1999.